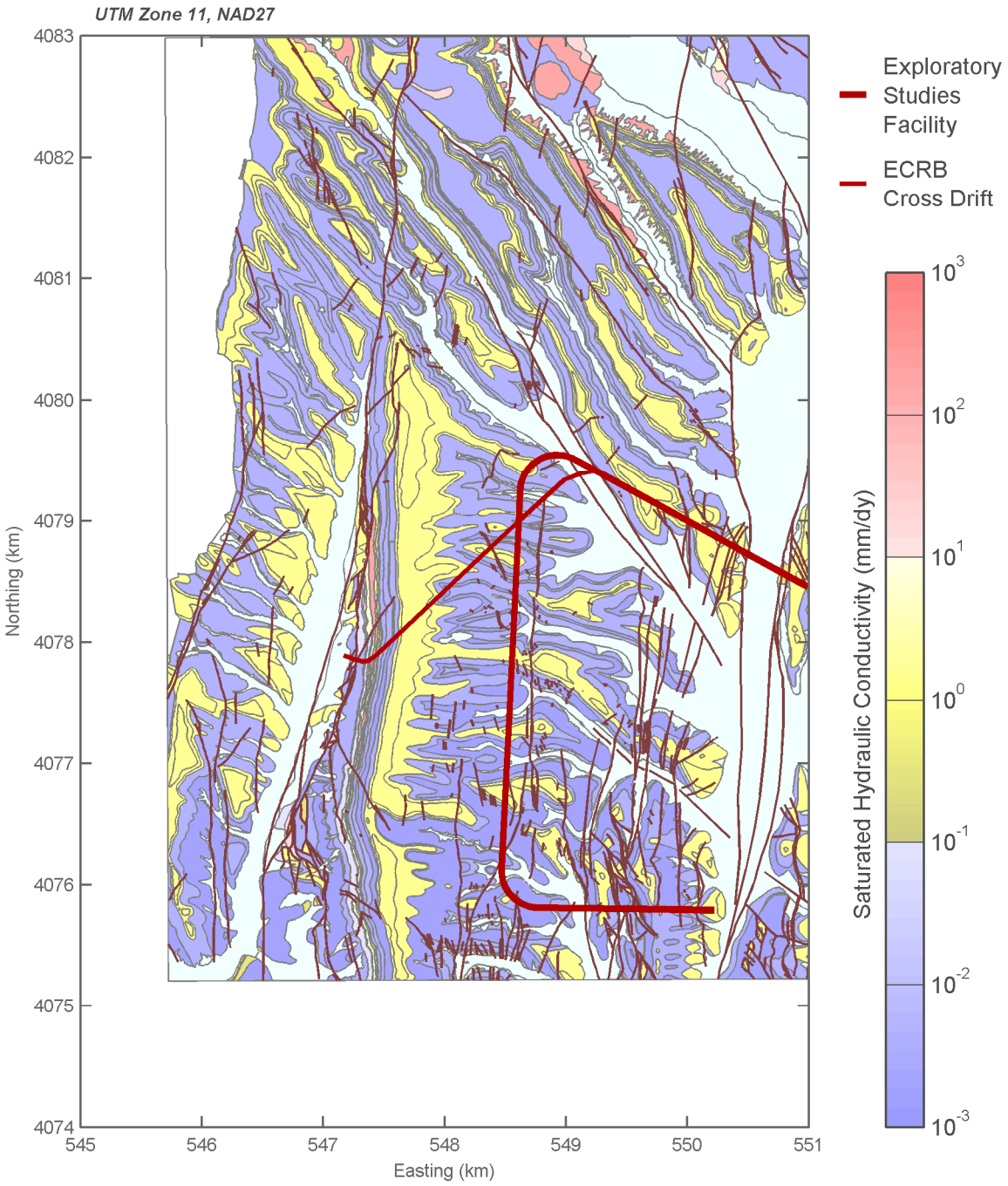

Figure 6-6. Independently Estimated Median Bedrock Saturated Hydraulic Conductivity Using the Flint (1998) Measurements. Areas in Pale Blue Use the Deep Soil Abstraction. [100 mm/day = 3.94 in/day]

hydraulic unit. In addition, there is a general trend for a slight reduction in K_{sat} relative to the ITYM set, with a number of units dropping from the low end of the transition range into the blue range or the low end of the high range into the transition range and other units moving lower in the transition range.

The independent NRC estimates were derived by considering regression relationships using each one-, two-, and three-parameter combination of measured properties to estimate $\log_{10}(K_{sat})$ simultaneously for all subsamples. Figure 6-7 shows the scatterplot of observed versus estimated K_{sat} values for the one-, two-, and three-parameter regressions with the largest coefficient of determination (R). For comparison, Figure 6-7(a) shows the scatterplot using the Flint (1998) estimates. The two-parameter regression has a significantly larger R than the one-parameter regression (more variability is explained), but adding a further parameter has a much smaller effect. The independent NRC estimate shown in Figure 6-6 uses the two-parameter regression shown in Figure 6-7c.

The two-parameter estimate with largest R value relates core sample K_{sat} to corrected saturation and subsample porosity; the one-parameter estimate with largest R value also had corrected saturation as the predictor for saturated hydraulic conductivity. Flint (1998) derived the corrected saturation values to account for evaporation during sample handling. The independent analysis derived the relationship.

$$\log_{10}(K_{sat}) = -7.779 - 4.194\theta_c + 7.568\varepsilon_{sample} \quad (6\text{-}1)$$

where

K_{sat} — saturated hydraulic conductivity [m/s]
θ_c — "corrected" sample saturation
ε_{sample} — subsample porosity

The explained variability between measured and estimated values (R^2) is 0.71 for the two-parameter estimate and 0.60 for the Flint (1998) estimate, visually indicated by a narrower band of scatter in Figure 6-7. The intermediate range of the independent estimates appears to be biased to the low side based on the scatterplot and is likely influenced by three high permeability outliers and the sample measurement limits evidenced by the vertical band at the low end of the observations. The general lowering of K_{sat} in Figure 6-6 may be at least partially an artifact of the regression bias.

Figure 6-8 further compares the Flint (1998) estimates and the two-parameter estimate. The six units at the top of the Tiva Canyon formation (Tcr1, Tcr2, Tcrn3, Tcrn4, Tcpul, and Tcpmn), which are prevalent within the potential-repository footprint, are used for the comparison. The first four units are found in the caprock, which is underlain by the upper lithophysal unit (Tcpul) and the middle nonlithophysal unit (Tcpmn). Each of the figure triplets represents one of the units, with a triplet indicating all possible combinations of corrected saturation, porosity, and $\log_{10}(K_{sat})$. Each large cyan dot denotes a measurement on a K_{sat} subsample (i.e., a core subsample used to measure K_{sat}). Each red circle denotes a core sample, with properties measured (for saturation and porosity) or estimated (for K_{sat}) by Flint (1998). Each small blue dot represents a single realization of core sample properties using the independent methodology (to help visualization, only 1 in 20 realizations is shown,). The large yellow circles with crosses represent mean values, with the cross colored to correspond to the estimate

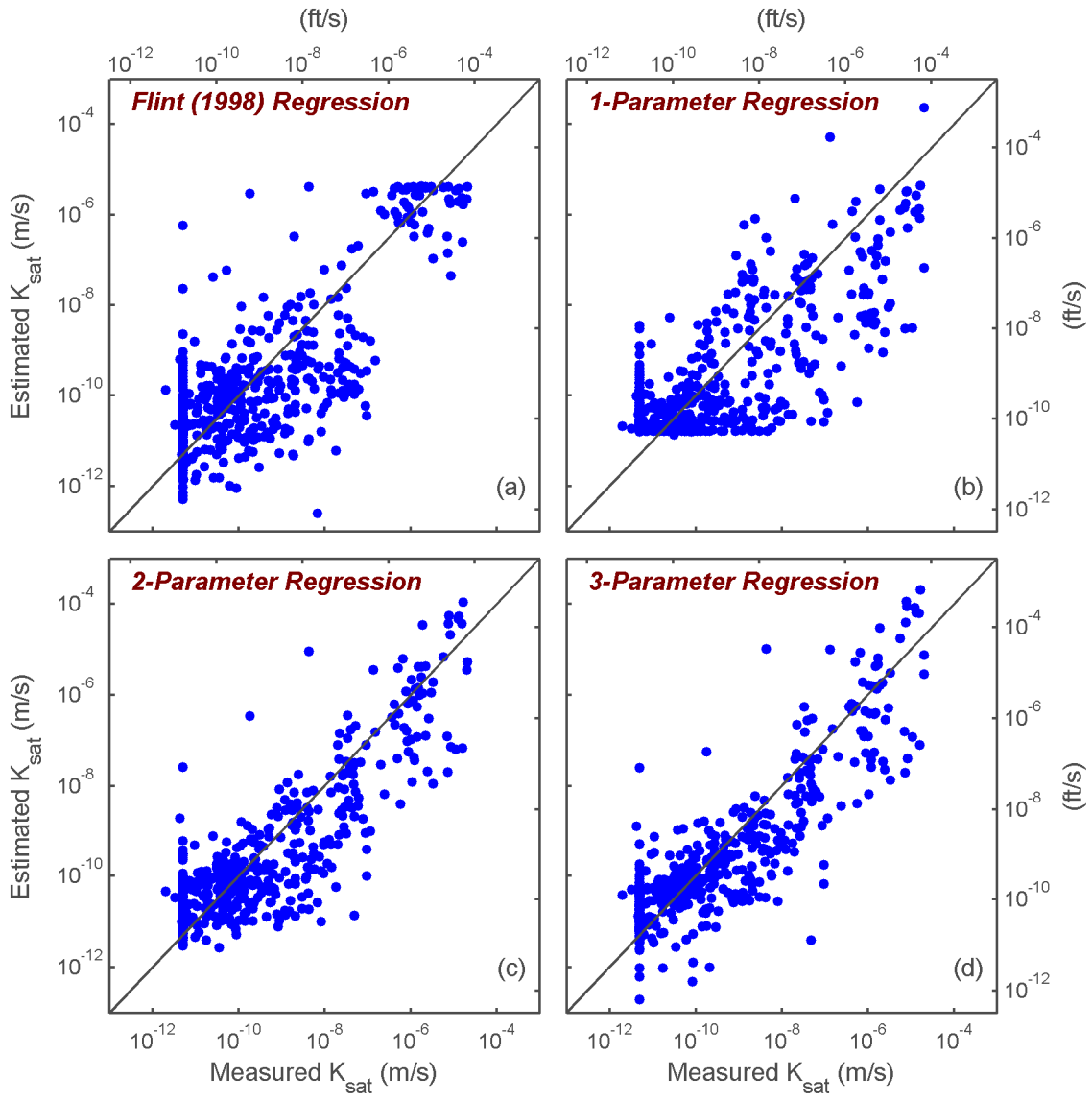

Figure 6-7. Estimated K_{sat} Compared to Measured K_{sat} for the Core Sample Database. (a) The Flint (1998) Regression and the (b) 1-Parameter, (c) 2-Parameter, and (d) 3-Parameter Regressions Yielding the Smallest Objective Function.

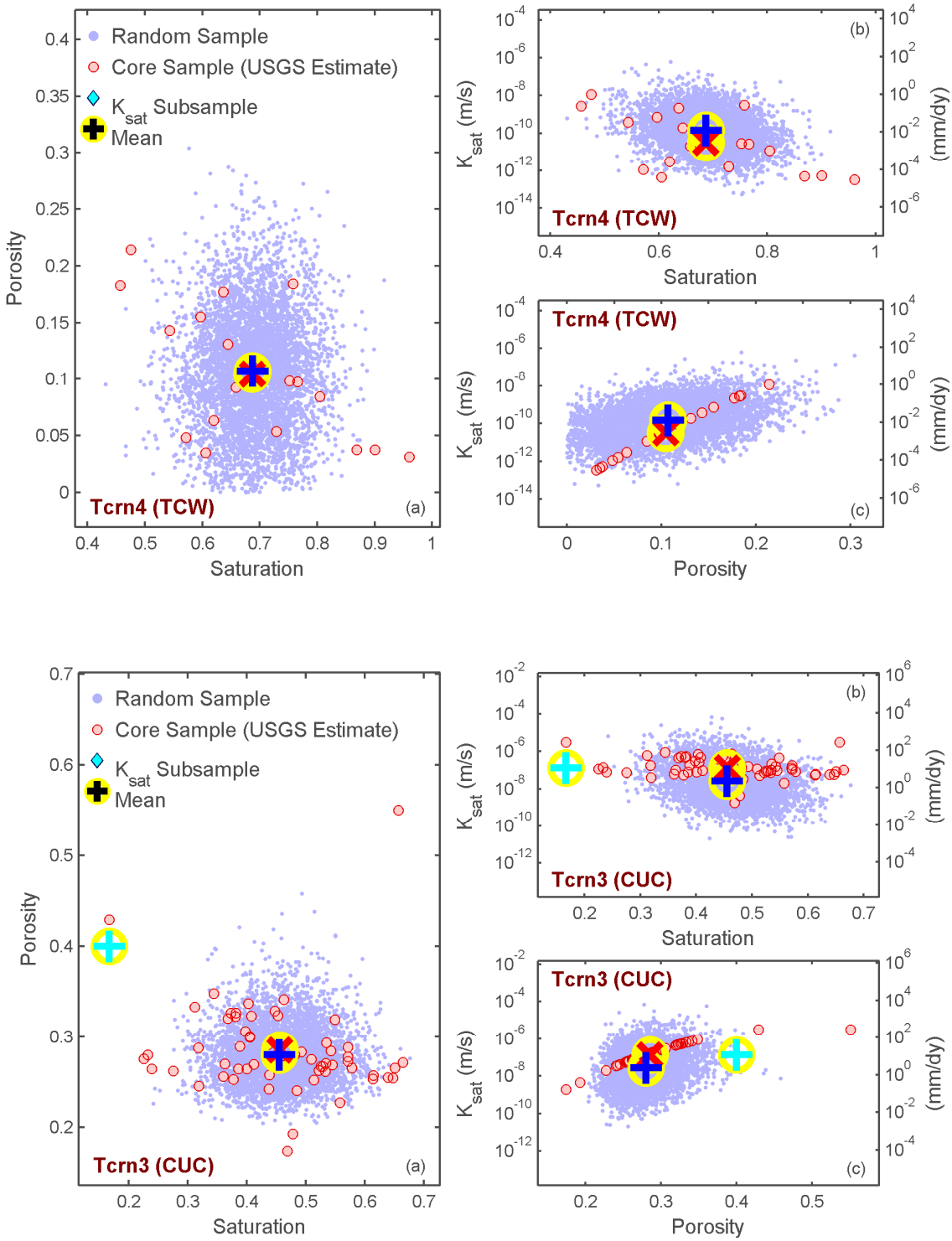

Figure 6-8. Scatterplots of (a) Saturation/Porosity, (b) Saturation/K_{sat}, and (c) Porosity/K_{sat} for Selected Units

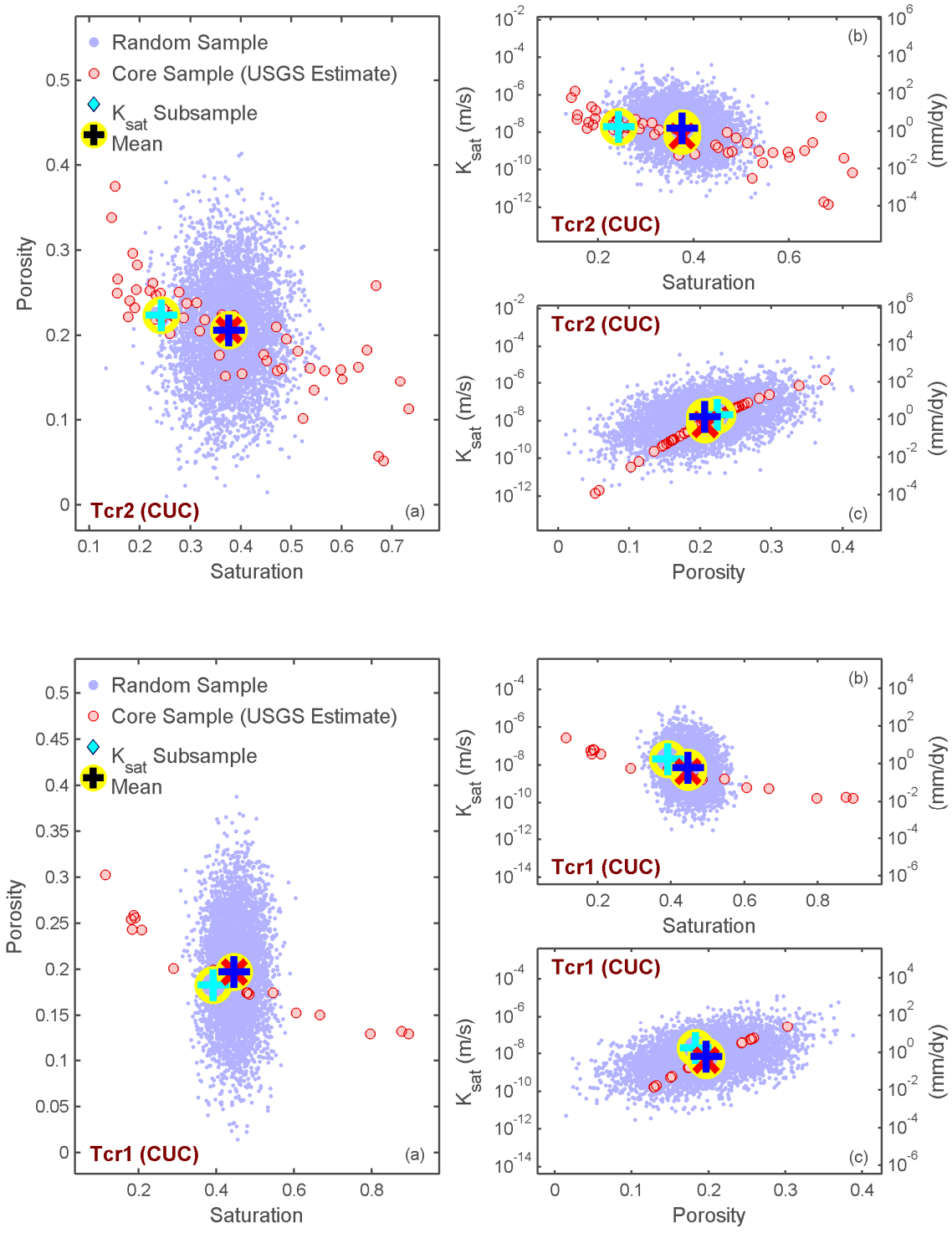

Figure 6-8 (continued). Scatterplots of (a) Saturation/Porosity, (b) Saturation/K_{sat}, and (c) Porosity/K_{sat} for Selected Units

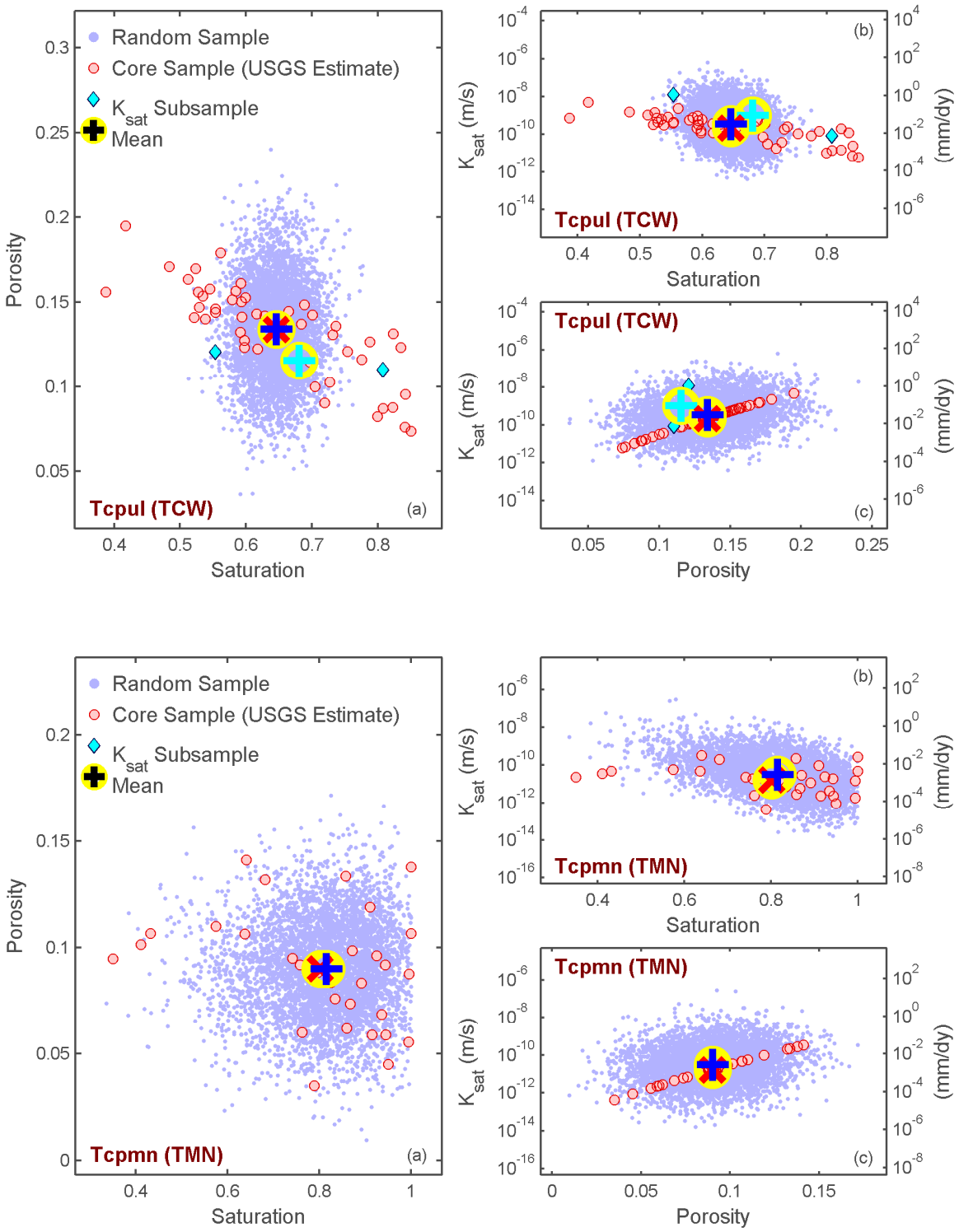

Figure 6-8 (continued). Scatterplots of (a) Saturation/Porosity, (b) Saturation/K_{sat}, and (c) Porosity/K_{sat} for Selected Units

source. The Tcpul unit has two K_{sat} subsamples; the Tcr1, Tcr2, and Tcrn3 units have one subsample; and the Tcrn4 and Tcpmn units have no subsamples. Units closer to the potential repository horizon have far more subsamples, so the regressions for the near-surface units are primarily based on units far from the ground surface and associated weathering processes.

The independent realizations generally spanned the range of porosity values for each unit except for the Tcrn3 unit. In general, the observed range of saturation values was wider than the span of realizations. The observed K_{sat} subsamples tend to have properties typical of the other cores, except that the sole Tcrn3 K_{sat} observation appears to be an outlier. Except for Tcrn3, the difference between the mean of the Flint (1998) estimates and the independent estimates is considerably smaller than the range in estimates over the set of cores.

Both sets of alternative estimates generally support the values used in the ITYM simulations, particularly within the potential repository footprint. Both sets of alternative estimates suggest that a relatively thin caprock unit along ridgetops, which ITYM describes as lying in the K_{sat} transition zone with some bedrock infiltration, may actually have bedrock K_{sat} sufficiently low to preclude significant infiltration. Areal-average MAI over the repository footprint would not be expected to drop by even as much as a factor of two due to reclassifying the unit, even in the absence of fracture pathways, because the unit was classified with a smaller K_{sat} (implying lower values of MAI) and has less than half of the outcrop area of other caprock units.

6.2.2 Bedrock Fracture Volume Fraction

Fracture properties affect estimates of MAI in two primary ways. Hydraulic properties of individual fractures, which are determined by the fill material in the fracture, determine flow rates for each fracture, while the areal average fracture volume fraction determines the areal average flow through the fractures. These properties have not been examined in detail and thus are

subject to a great deal of uncertainty. Section 6.2.2 describes the fracture volume fraction input to ITYM and the ITYM sensitivity to fracture volume fraction, and Section 6.2.3 describes the properties of the media in the fractures.

Bulk saturated hydraulic conductivity of the fractures used in ITYM simulations is estimated by assuming that fractures were partly filled with soil, partly filled with carbonate, and partly unfilled. The Flint, et al. (1996a, Table 2) estimated fracture density and fracture aperture categories were used to estimate the overall volume fraction of void space for most units. Assigned fracture apertures varied by unit, with apertures generally assumed to be 25 μm [0.00098 in] in most units but 250 μm [0.0098 in] in densely welded nonlithophysal units. Void space in the caprock is estimated differently, because weathering tends to form large-aperture, soil-filled joints between massive blocks that function as the primary infiltration pathway. Caprock tuff blocks are estimated to be on the order of a meter on a side, with joint apertures of a few centimeters.

The relative proportions of carbonate-, soil-, and unfilled fractures were qualitatively assigned based on limited field observation. Densely welded units were generally assumed to be predominately carbonate filled, with some portion assumed unfilled and a lesser portion assumed soil filled. Nonwelded tuffs were generally assumed to be filled with carbonate and soil in equal proportions, with a slightly larger proportion considered unfilled. Densely welded nonlithophysal units were assumed to be predominately soil filled, with some portion assumed

carbonate filled and a lesser portion assumed unfilled, based on limited observations of the Tcpmn unit exposed at several locations where weathering and root penetration further broke up the welded joint-bounded blocks.

MAI is highly sensitive to fracture volume fraction in the ITYM abstractions and is also quite sensitive to hydraulic properties of both the overlying soil and the fracture fill. The sensitivity of MAI to fracture volume fraction is illustrated using a soil-filled system, which has properties intermediate between unfilled and carbonate-filled systems. An unfilled fracture system has larger saturated hydraulic conductivity than the corresponding soil-filled system but provides a capillary barrier, and MAI is strongly affected by soil thickness. In terms of bulk permeability, filled fractures in a low permeability matrix represent a permeability barrier, because the volume fraction of the fracture system is small. Carbonate fill tends to have lower permeability and finer texture than soil fill; thus it is an even stronger permeability barrier.

The capillary properties of the soil and the different fracture classifications also play a role. The smaller the pores in a porous medium, the stronger the capillary forces for the porous medium. A fine medium in a fracture, such as carbonate fill, will tend to accept water from a coarser medium, such as the overlying soil column, at lower saturations than a coarser medium in the fracture. Accordingly, a given wetting pulse will enter a carbonate-filled fracture for longer durations than a soil-filled fracture and may not induce flow at all in an unfilled fracture.

These sensitivities are illustrated for present-day climatic conditions (representative of Desert Rock, Nevada) in Figures 6-9 and 6-10, which indicate sensitivity to hydraulic properties, for a profile with shallow soil overlying a soil-filled fracture system. The three subfigures in Figures 6-9 and 6-10 represent three different fracture volume fractions, labeled with illustrative fracture characteristics that would produce the same volume fraction. The upper and lower values for each illustrated property represent one standard deviation about the mean using the ITYM input set. The curves denoted $+\sigma$ and $-\sigma$ represent MAI when all properties are set to plus and minus one standard deviation (the van Genuchten P_o parameter is assigned the opposite sign as the other properties for these curves because it tends to be negatively correlated with the other properties). Figure 6-9 illustrates that MAI estimated by the abstraction is relatively insensitive to fracture volume fraction for very high values of volume fraction and is quite sensitive for somewhat lower values. This large sensitivity may be partially an artifact of the abstraction process, because few simulations with intermediate fracture volume fractions were used to derive the abstractions. Note that the volume fraction in Figure 6-9(c) is 0.02, whereas the median estimated volume fraction is less than 0.005 for all units other than the caprock units using the ITYM input values. Also note that the soil retention properties have a large influence on MAI, especially at lower values of fracture volume fraction. Smaller values for both soil k_s and van Genuchten P_{os} increase MAI. Further, a change in a soil hydraulic parameter results in a change to the slope of MAI versus soil thickness plotted in log-log coordinates.

Figure 6-10 shows a somewhat reduced sensitivity to fracture hydraulic parameters relative to soil hydraulic parameters. In contrast to soil parameters, a change in a fracture property acts as a multiplier for MAI that does not change the slope of the corresponding MAI line plotted in log-log coordinates. Further, the sensitivity to fracture hydraulic properties has the opposite sign relative to the soil hydraulic properties. Note that the σ curves lie within the curves denoting one standard deviation of K_f because P_{of} is assigned the opposite sign from the remaining properties, thus countering some of the variability.

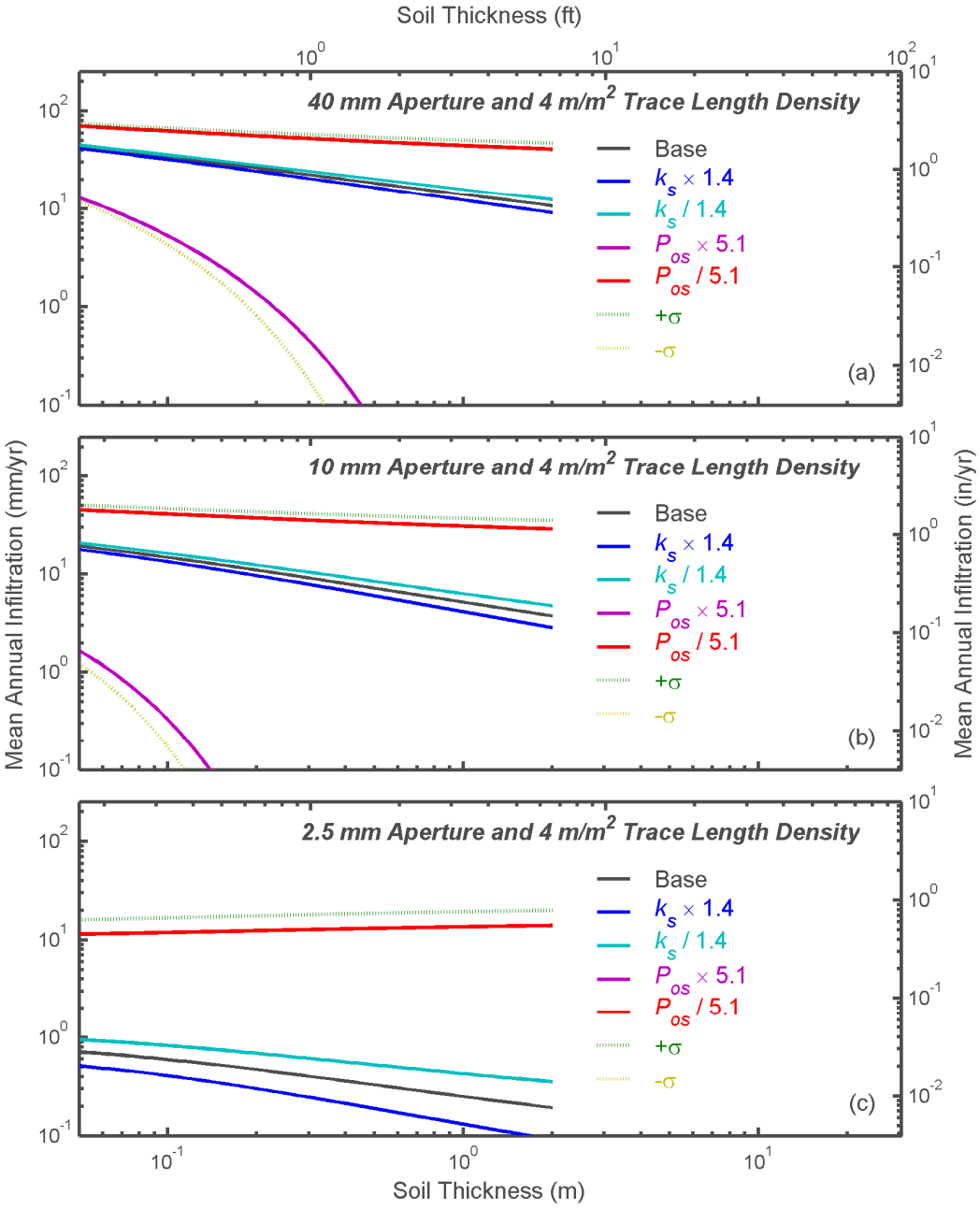

Figure 6-9. Abstracted Mean Annual Infiltration for Various Hydraulic-Property Combinations for the Overlying Soil in a System With Bare Soil Overlying a Soil-Filled Fracture System for Volume Fractions of (a) 0.16, (b) 0.04, and (c) 0.01. The Range in Hydraulic Properties Represents ±1 Standard Deviation in ITYM Simulations. The σ Values Represent All Four Hydraulic Properties at ±1 Standard Deviation, With P_{os} Having the Opposite Sign From the Other Three.

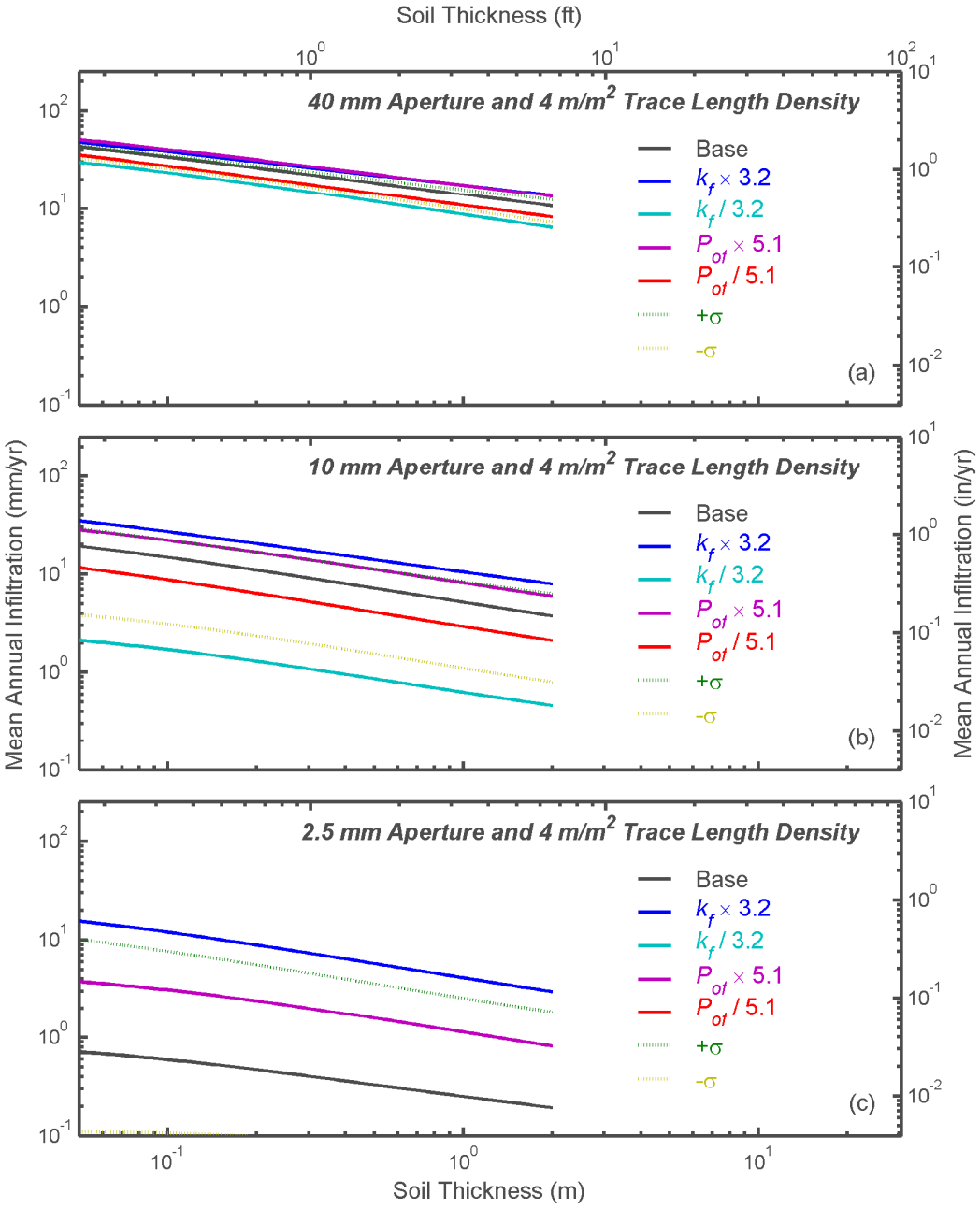

Figure 6-10. Abstracted Mean Annual Infiltration for Various Hydraulic-Property Combinations for the Underlying Soil Fill in a System With Bare Soil Overlying a Soil-Filled Fracture System for Volume Fractions of (a) 0.16, (b) 0.04, and (c) 0.01. The Range in Hydraulic Properties Represents ±1 Standard Deviation in ITYM Simulations. The σ Values Represent All Four Hydraulic Properties at ±1 Standard Deviation, With P_{of} Having the Opposite Sign From the Other Three.

Figures 6-9 and 6-10 suggest that a soil-filled fracture with nominal hydraulic properties would have estimated MAI less than 1 mm/yr [0.04 in/yr] if the corresponding fracture volume fraction is less than 0.02. The CUC aggregated hydraulic unit is the only merged hydraulic property set with such a large fracture volume fraction in the ITYM model input. Flint, et al. (1996a) assign the CUC aggregated hydraulic unit to the Tcr1, Tcr2, and Tcrn3 Tiva Canyon caprock units, whereas U.S. Geological Survey (2001) assigns the CUC aggregated hydraulic unit to just the Tcr2 and Tcrn3 units. Note that the combination of spatial variability and uncertainty in ITYM hydraulic properties results in a significant calculated probability that MAI will be greater than 1 mm/yr [0.04 in/yr] even for fracture volume fractions significantly less than 0.02.

Figure 6-11 displays the median fracture volume fraction used in ITYM simulations. Red tones indicate large fracture volume fractions where nominal MAI for soil-filled fractures is significant (based on Figure 6-9). Blue tones indicate very small fracture volume fractions where nominal MAI is essentially zero. Yellow tones indicate intermediate fracture volume fractions. In general, red tones indicate areas where ITYM would frequently estimate bare-soil MAI greater than 1 mm/yr [0.04 in/yr] if the fractures were filled with soil, yellow tones indicate areas where ITYM would occasionally estimate bare-soil MAI greater than 1 mm/yr [0.04 in/yr] if the fractures were filled with soil, and blue tones indicate areas where ITYM would rarely estimate bare-soil MAI greater than 1 mm/yr [0.04 in/yr] if the fractures were filled with soil.

Figure 6-11 suggests that the caprock would be the primary location for net infiltration to occur. The hydraulic unit mapping by U.S. Geological Survey (2001) exhibits similar patterns as the Flint, et al. (1996a) mapping, except the stratigraphically lowest caprock unit is in the blue zone. Figure 6-12 shows a revised independent estimate, using pavement maps and the ESF detailed line survey. The revised estimate again indicates that the caprock is most likely to exhibit significant MAI, but other units may have a higher probability of significant MAI.

6.2.3 Bedrock Fracture Hydraulic Properties

Near-surface fractures at Yucca Mountain are usually filled with either the fine component of the overlying soil or a mixture of calcium carbonate and siliceous materials. There has been little or no quantification of the relative distributions of the different fillings in the near-surface environment. Field observation suggests that calcium carbonate/silicate fracture fill may be prevalent in areas with relatively fine and infrequent fractures, such as the lithophysal units of the Tiva Canyon welded formation. Soil fillings are more evident in units with relatively large-aperture fractures and fissures, such as caprock and nonlithophysal zones of the Tiva Canyon welded unit, although it is possible that carbonates appear at depth in fractures that have soil fillings near the soil/bedrock interface. Unfilled fractures are common in the Paintbrush Tuff nonwelded units, although little evidence of flow through the fractures is evident (Moyer, et al., 1996). In welded tuff, however, unfilled fractures may be rare. Even apparently unfilled fractures in well-washed areas of welded tuff such as active bare-rock channels in Split Wash appear to have fill below the channel bottom, based on observations of extremely slow drainage rates from ponded waters (Stothoff, 2008).

Field observations from several expeditions (Stothoff, 2008) suggest the texture of soil fill is similar to the overlying soil; thus it would be expected that the hydraulic properties of soil fillings are similar to the fine component of the overlying soil.

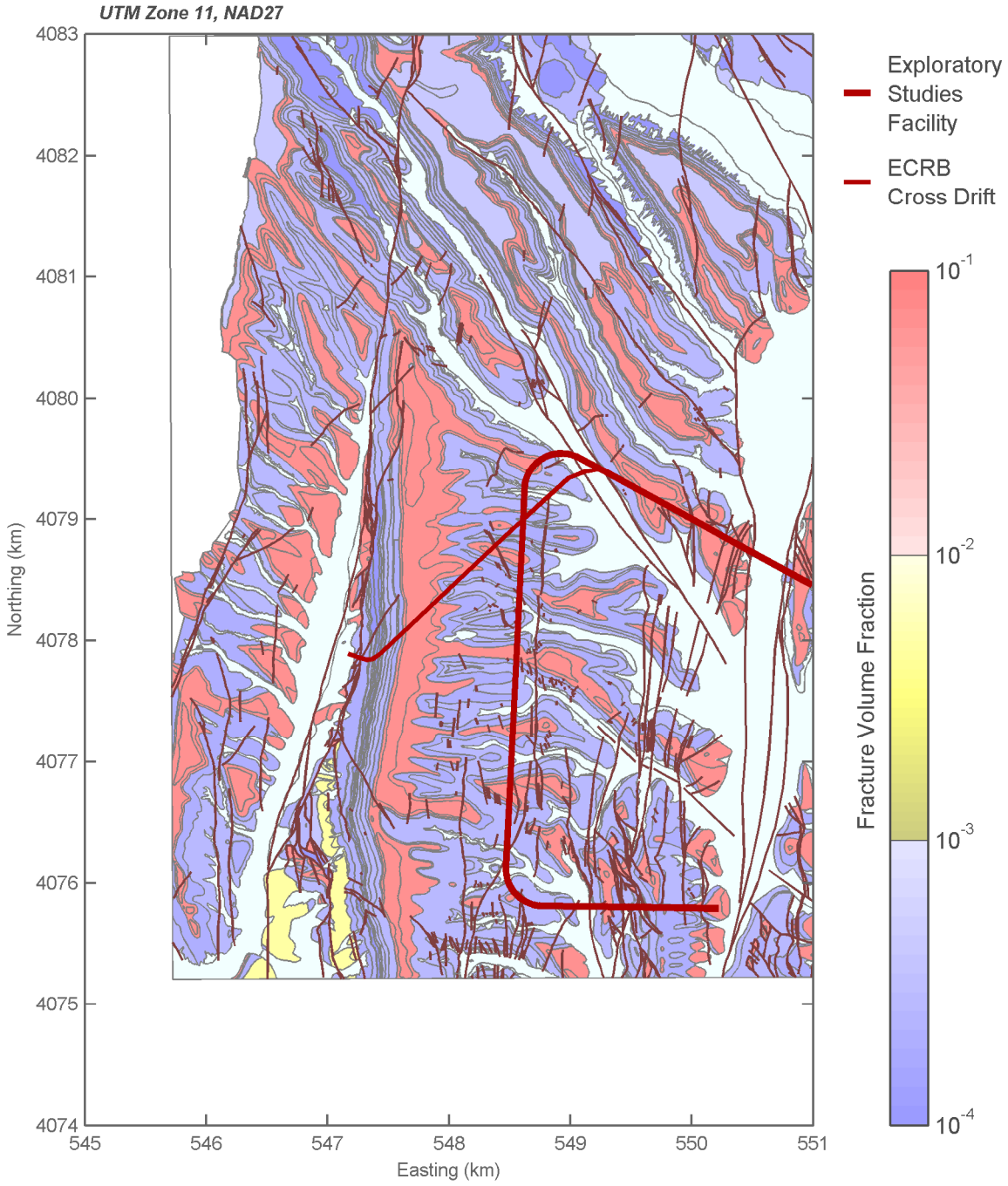

Figure 6-11. Median Fracture Volume Fraction Used by Infiltration Tabulator for Yucca Mountain. Areas in Pale Blue Use the Deep Soil Abstraction.

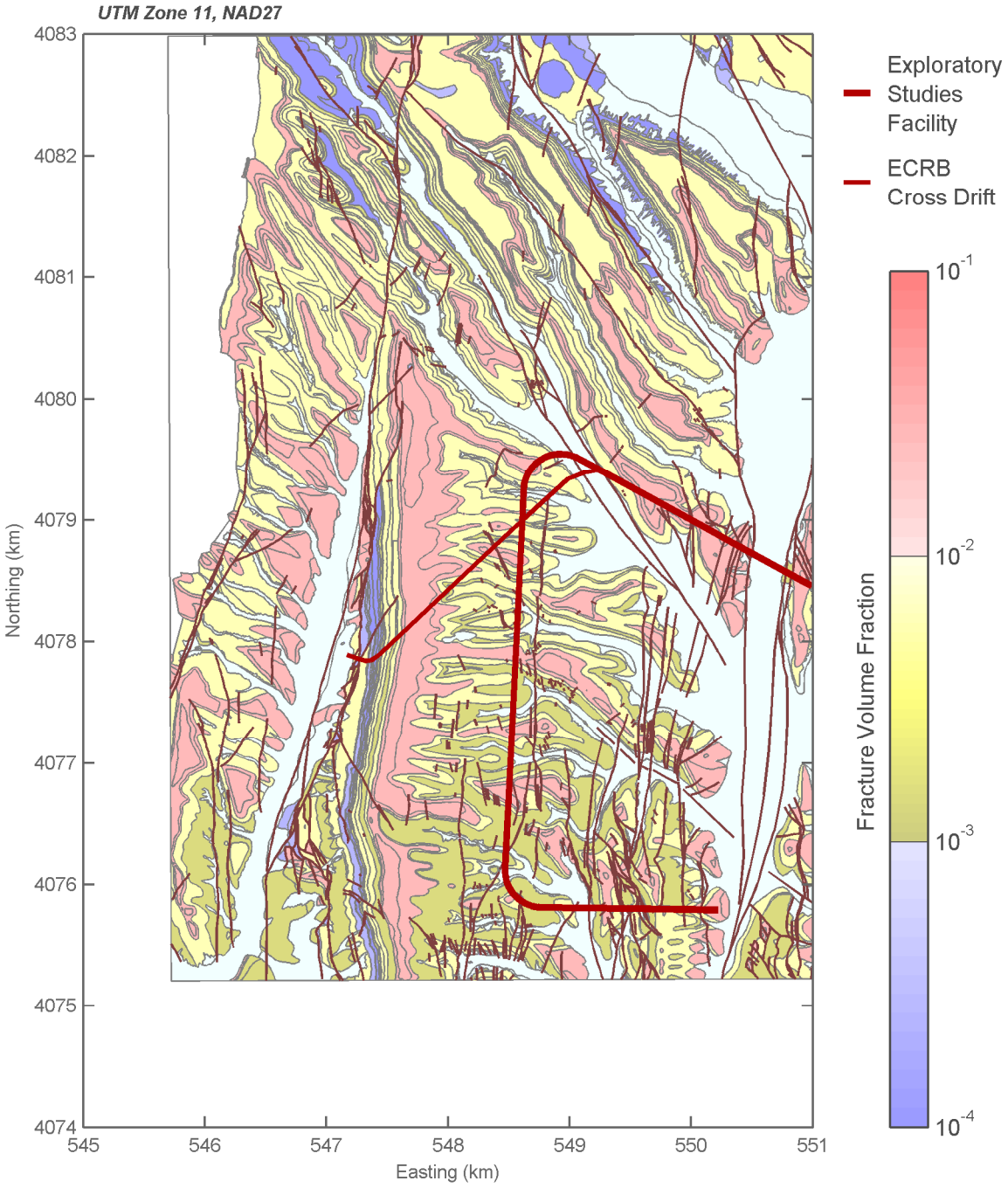

Figure 6-12. Median Fracture Volume Fraction Based On Independent Analysis. Areas in Pale Blue Use the Deep Soil Abstraction.

The properties of carbonate and silicate fillings have not been examined in detail, in part because it is difficult to extract undisturbed samples of fracture fillings. Saturated hydraulic conductivity values are shown in Figure 6-13 for a small number of fill samples the U.S. Geological Survey analyzed for DOE (U.S. Geological Survey, 1997). The analyses were performed both perpendicular to the fracture plane and along the fracture plane. Water may move relatively easily along the fractures and may be restrained from entering the matrix (depending on capillary contrasts between the fill and matrix), because all but 1 of the 11 across-fracture samples has a K_{sat} value that is 1 to at least 7 orders of magnitude smaller than the K_{sat} values typical of the 4 along fracture samples. Flint, et al. (1996a) and U.S. Geological Survey (2001) used 5×10^{-7} m/s [43.2 mm/d or 1.7 in/d], which is the arithmetic mean of the samples, to represent fracture-fill K_{sat}. The geometric mean of the along-fracture K_{sat} is slightly larger: 1.4×10^{-6} m/s [120 mm/d or 4.7 in/d]. Note that the model of Flint, et al. (1996a) does not require retention properties for fracture materials.

Baumhardt and Lascano (1993) measured the hydraulic properties of a caliche layer near Lubbock, Texas, finding that the vertical and horizontal means (using the logarithm) for saturated hydraulic conductivity were 8.72×10^{-6} and 2.26×10^{-5} m/s [30 and 77 in/day], respectively (shown in Figure 6-13). These sets of values are somewhat larger than the along-fracture values the U.S. Geological Survey measured. Baumhardt and Lascano (1993) described the retention properties of the caliche layer with van Genuchten parameters $\alpha = 3.555$ kPa^{-1} and $n = 1.271$, which is consistent with a clay texture. The measured samples

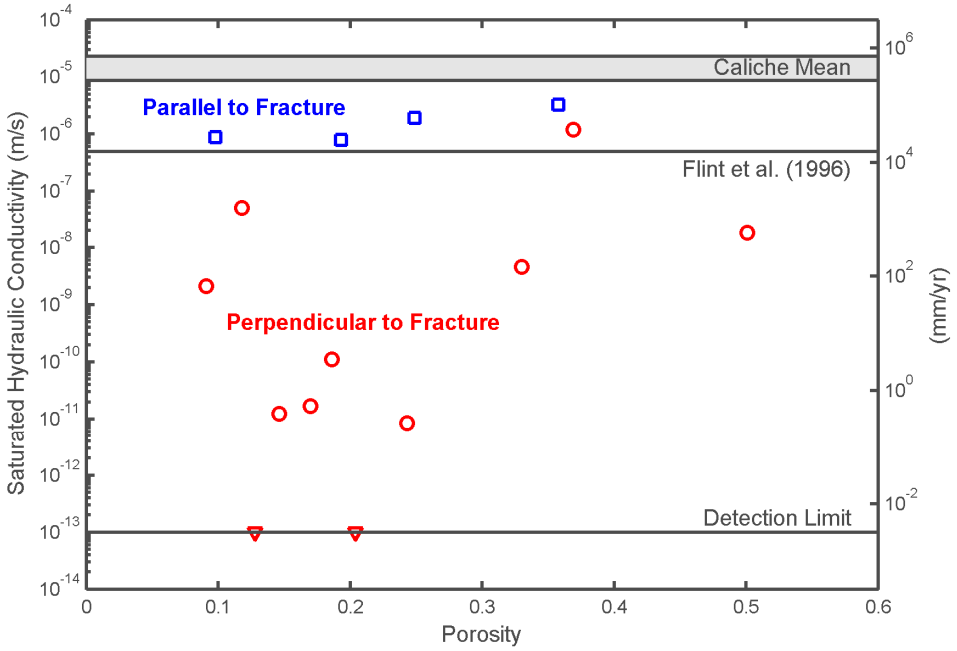

Figure 6-13. Saturated Hydraulic Conductivity for Samples of Fracture-Fill Material. Along-Fracture Conductivity Is Consistently Greater Than 10^{-6} m/s [1,200 in/yr], While Across-Fracture Conductivity May Be Many Orders of Magnitude Smaller. The Vertical and Horizontal Geometric Mean of the Baumhardt and Lascano (1993) Caliche Data Set Are Indicated by the Shaded Area. The Value Used by Flint, et al. (1996a) Is the Arithmetic Average of the Sample Values.

and the caliche data suggest that K_{sat} in carbonate-filled fractures may be between the arithmetic average and the Baumhardt and Lascano (1993) values. At the higher end of the K_{sat} range, retention properties are likely similar to clay, but retention properties at the lower end of the K_{sat} range have not been determined. There is considerable uncertainty regarding this parameter, however, and it is not clear how to incorporate the data on across-fracture K_{sat}. Presumably, the low across-fracture K_{sat} values would limit matrix–fracture exchange consistent with the one-dimensional simulations with no matrix–fracture exchange used to develop the ITYM abstractions.

Some of the fractures may not be filled, and fill material often ceases to exist at some depth into the bedrock. Near-surface unfilled fractures are likely to have a narrow aperture, or else soil would enter. Hydraulic properties of unfilled fractures can be estimated using the parallel plate assumption, which relates fracture K_{sat} to the cube of aperture. Unfilled fracture retention properties are typically modeled as a very coarse material such as gravel. However, one-dimensional simulations of infiltration that considered soil over unfilled fractures found that MAI is not sensitive to fracture properties, except when there are few fractures (Stothoff, 1997). The lack of sensitivity is because (i) a strong capillary barrier effect limits flow from the soil to the fracture unless the soil is essentially saturated and (ii) the typical fracture permeability is so large that drainage into fractures is controlled by the ability of the soil to deliver water to the fracture.

Figure 6-14 displays the median bulk saturated hydraulic conductivity of the filled fractures used in ITYM simulations, estimated by multiplying the fracture volume fractions discussed in Section 6.2.2 by the K_{sat} estimates discussed in this section. The contribution of the unfilled fractures is not shown, because the abstractions suggest that MAI due to open fractures is reduced dramatically under present climatic conditions with a relatively shallow soil cover. The color scale from Figures 6-5 and 6-6 is also used to describe fracture conductivity. The caprock areas are in the red range, indicating that fracture hydraulic conductivity does not limit MAI in the ITYM simulations, and densely welded nonlithophysal units with the same hydraulic properties as the Ttpmn unit of the Topopah Spring welded tuff are in the yellow range, indicating that the fracture system partially constrains MAI. Note that if the Tcpmn unit (the Tiva Canyon middle nonlithophysal unit) was provided with the same fracture description as the Ttpmn unit (the Topopah Spring middle nonlithophysal unit), much of the area shaded in blue in the southern quarter of the Day, et al. (1998) region shown in Figure 6-14 would fall into the upper end of the yellow range.

U.S. Geological Survey (2001) estimated bulk saturated hydraulic conductivity for the fracture system. The fracture volume fraction used by U.S. Geological Survey (2001) is generally somewhat larger than the fracture volume fraction used in ITYM simulations (except in the caprock units), but the U.S. Geological Survey (2001) fracture hydraulic conductivity is in the blue range or the extreme low end of the yellow range in all units, suggesting that the fracture system contributes essentially nothing to areal-average MAI. The ITYM simulations have a larger fracture conductivity than the U.S. Geological Survey (2001) simulations, despite a smaller volume fraction, because a fraction of fractures are considered soil filled. The assumed hydraulic conductivity of soil in the fracture system is approximately two orders of magnitude greater than the assumed hydraulic conductivity of carbonate in the fracture system.

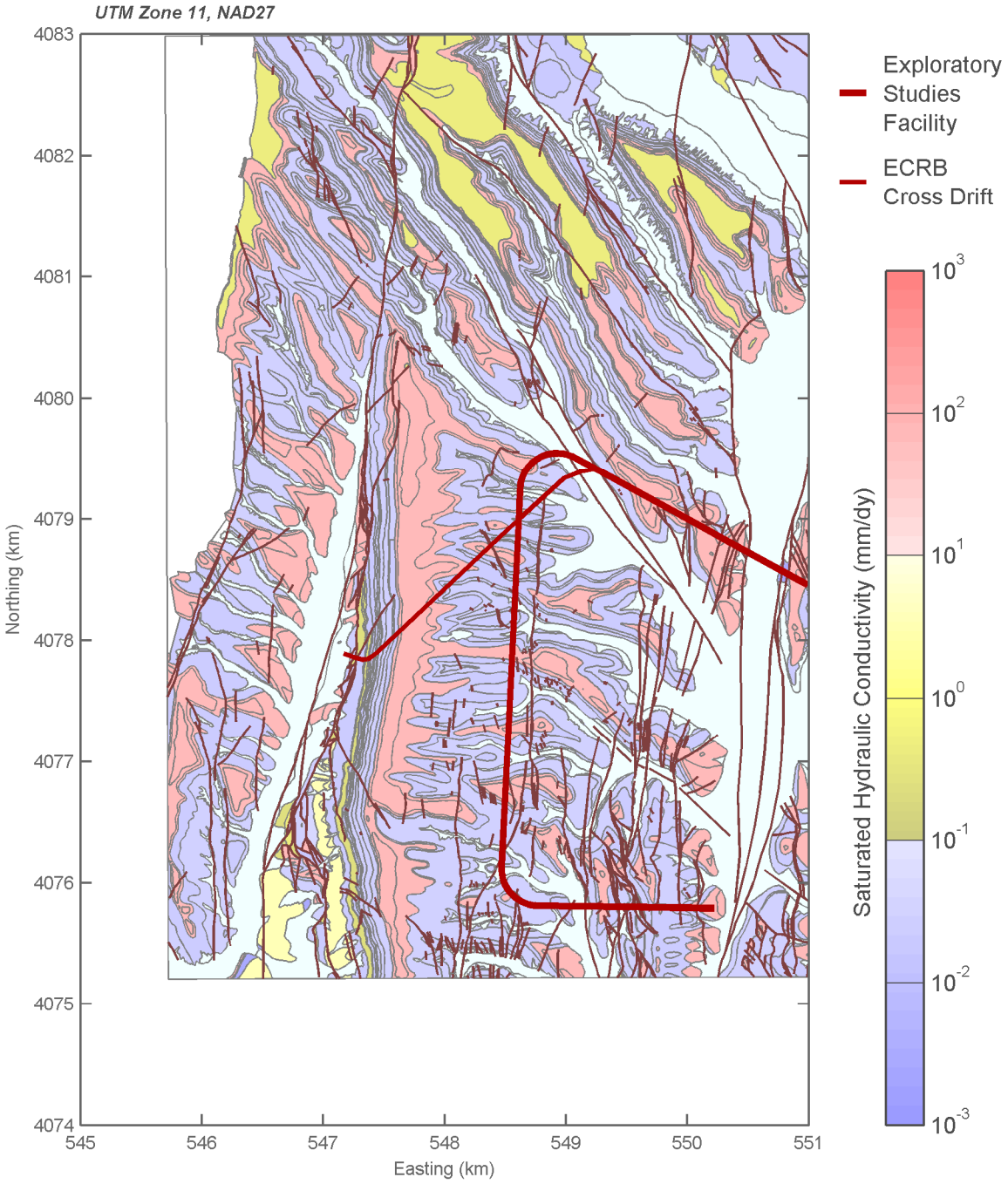

Figure 6-14. Median Filled-Fracture Saturated Hydraulic Conductivity Used by Infiltration Tabulator for Yucca Mountain. Areas in Pale Blue Use the Deep Soil Abstraction. [100 mm/day = 3.94 in/day]

Figure 6-15 displays estimates for bulk fracture K_{sat} based on independent NRC confirmatory calculations, drawing from infiltration experiments on Exile Hill above Alcove 1, pavement mapping within the upper lithophysal zone of the Tiva Canyon formation, and detailed line survey data for fracture properties within the ESF. At first glance, these independent confirmation calculations would appear to be significantly different from the estimates indicated in Figure 6-14, but the two sets of calculations are actually in good agreement in regard to the influence of bedrock properties on MAI. In both figures the caprock units of the Tiva Canyon formation do not limit MAI and essentially all remaining units either completely or strongly limit MAI. Perhaps the most substantive difference occurs in the southwest portions of the figures, where the independent calculations indicate that bulk K_{sat} drops by almost an order of magnitude in the Ttpmn and Tmrw exposures.

Figure 6-16 displays the porous component of the bedrock (i.e., bedrock matrix, carbonate-filled fractures, or soil-filled fractures) in the ITYM simulations that has the largest bulk hydraulic conductivity (i.e., hydraulic conductivity times component volume fraction). Areas with largest bulk conductivity in soil-filled fractures are indicated in yellow, and areas with largest bulk conductivity for the bedrock matrix are indicated in red. The carbonate-fill fraction does not appear on the map, because the soil-fill conductivity is approximately 100 times greater than the carbonate-fill conductivity, and soil is assumed to fill at least 10 percent of the fractures in every unit. Therefore, the bulk conductivity of the carbonate-filled fractures is less than the bulk conductivity of the soil-filled fractures everywhere in the domain.

A map using the material properties estimated by U.S. Geological Survey (2001) would replace yellow with red everywhere in the mapped area, indicating that the fracture system is less conductive than the bedrock matrix. On the other hand, the independently estimated material properties shown in Figures 6-6 and 6-12 suggest that this is the case only for exposures of nonwelded and moderately welded tuff. A map using the independently estimated properties replaces yellow with red in a few small scattered patches and replaces red with yellow almost everywhere in the southern half of the mapped area. Only exposures of nonwelded and moderately welded tuff exhibit bedrock matrix bulk conductivity larger than fracture bulk conductivity.

6.2.4 Confirmation of Bedrock Fracture Conductivity Estimates

Three Tiva Canyon formation units dominate the surface area above the potential repository: caprock (Tcr1, Tcr2, Tcrn3, and Tcrn4 units), the upper lithophysal unit (the Tcpul unit), and the middle nonlithophysal unit (the Tcpmn unit). Other units have small exposure area or are typically covered by deep soil. This section provides estimates of bulk fracture K_{sat} for these three units to illustrate the independent estimates of Figure 6-15.

Fracture pore volume in the caprock of the Tiva Canyon formation (i.e., the Tcr1, Tcr2, and Tcrn3 units) is estimated with the knowledge that the primary fracture volume is in the weathered cooling joints that separate massive blocks of bedrock. This configuration is typical of caprock on Yucca Crest, even underlying surficial deposits (Stothoff, et al., 1999). As a back-of-the-envelope estimate, the blocks are assumed to be 1.5 m [4.9 ft] on a side, with a

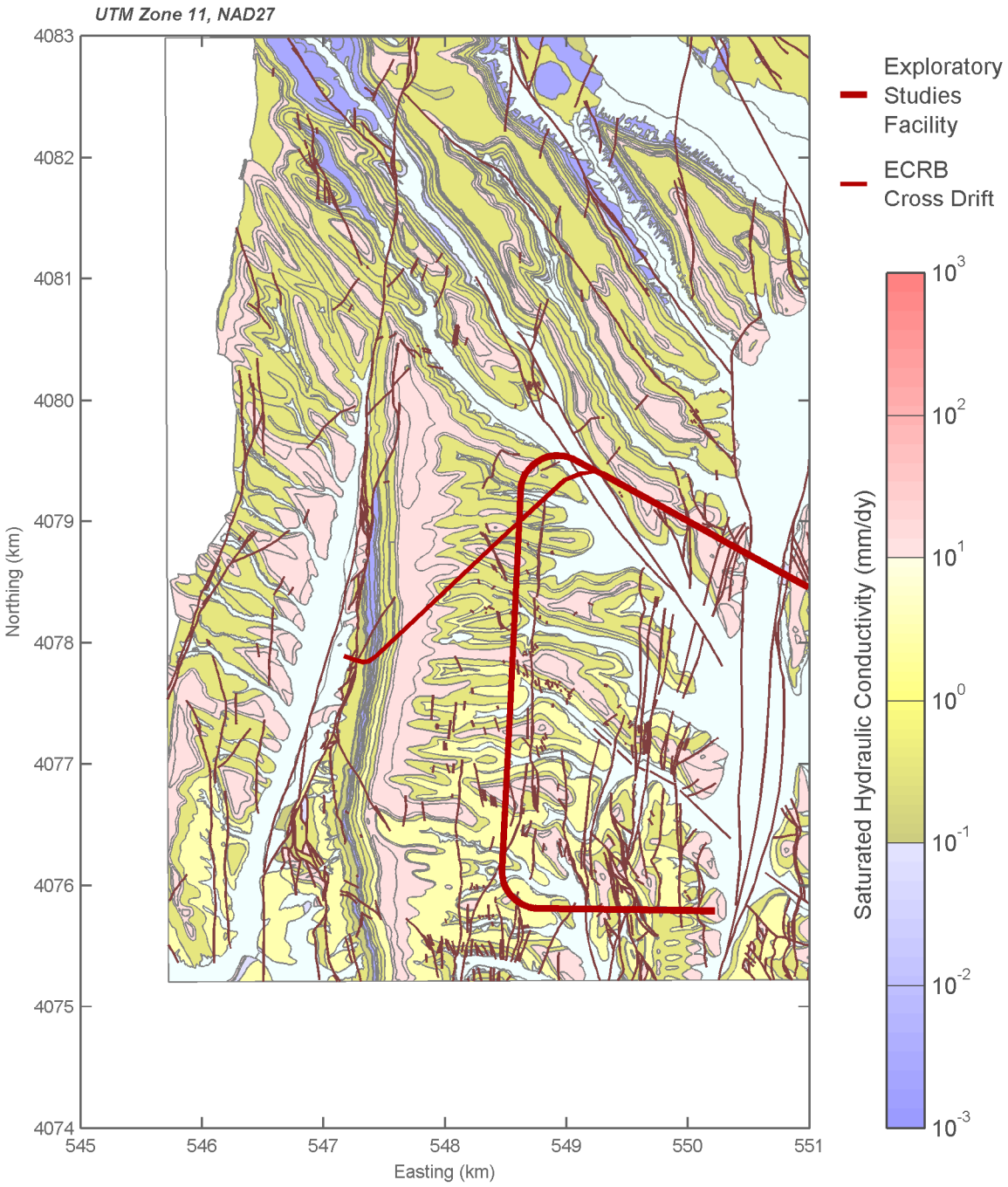

Figure 6-15. Median Filled-Fracture Saturated Hydraulic Conductivity Based on Independent Analysis. Areas in Pale Blue Use the Deep Soil Abstraction. [100 mm/day = 3.94 in/day]

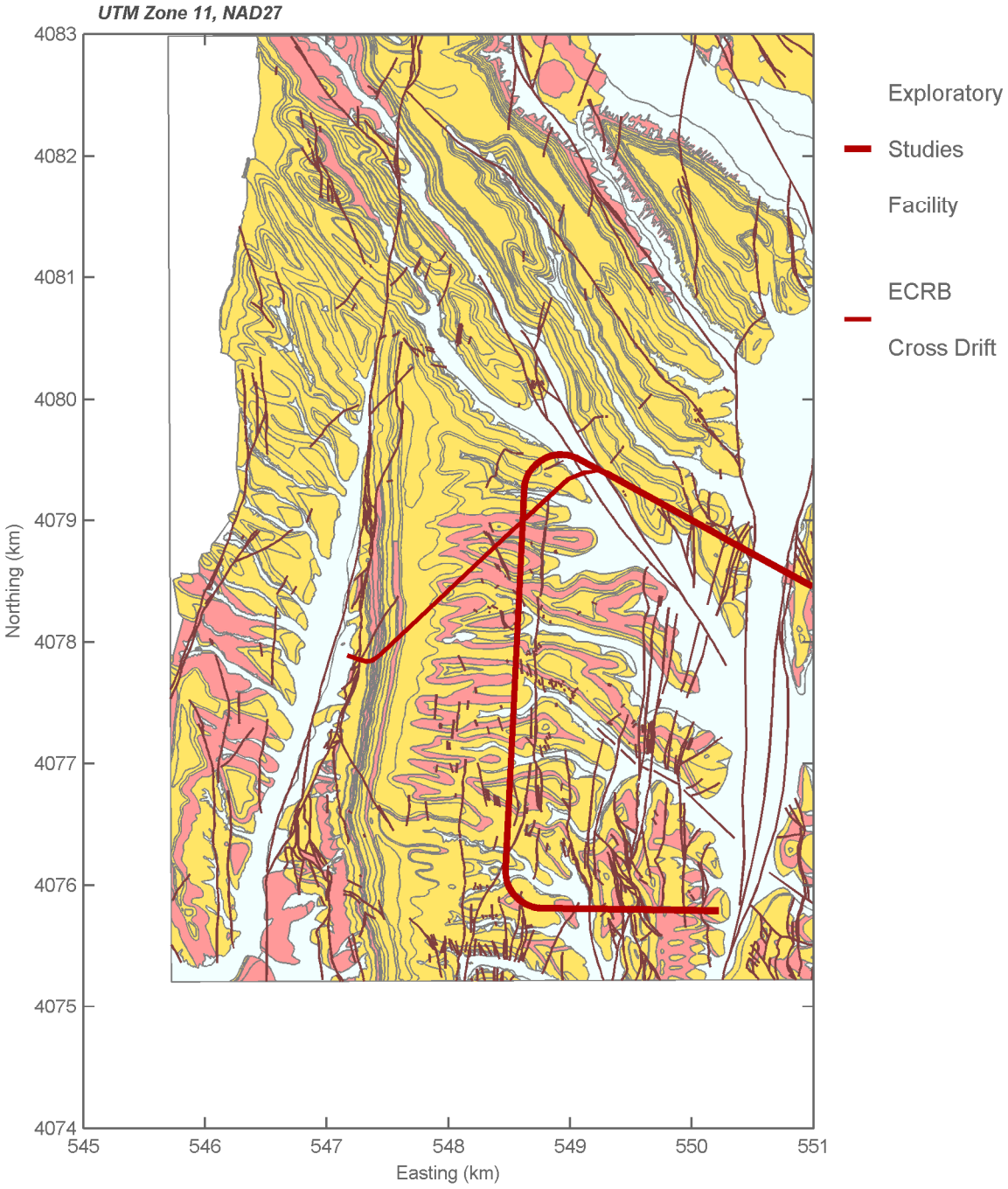

Figure 6-16. Bedrock Component With Largest Estimated Bulk Hydraulic Conductivity. Yellow Indicates Soil-Filled Fractures; Red Indicates Bedrock Matrix. No Location Has Carbonate-Filled Fractures Providing the Largest Bulk Conductivity. Unfilled Fractures Are Not Included.

2-cm [0.8-in] soil-filled joint surrounding each block, yielding a fracture void fraction of 0.0267. The void space is assumed to be essentially completely filled with fine soil having K_{sat} of 2 cm/hr [0.79 in/hr], typical of the fine eolian matrix, yielding a bulk K_{sat} of 13 mm/d [0.51 in/d]. This bedrock K_{sat} estimate is within the red range for K_{sat}, suggesting that bedrock K_{sat} does not limit MAI.

Field evidence suggests that the back-of-the-envelope estimate is within a factor of two to three inferred for a location above Alcove 1, but may somewhat underestimate field properties at this location. A factor of two to three is a reasonably close estimate for K_{sat}, because fracture K_{sat} in different units may be different by many orders of magnitude and generally varies spatially even within the same unit. Infiltration rates averaging greater than 20 mm/d [0.79 in/d] were maintained without ponding for more than 6 months in an infiltration experiment on Exile Hill above Alcove 1 (Liu, et al., 2003), with peak application rates exceeding 50 mm/d [2 in/d]. The Day, et al. (1998) map suggests that the infiltration plot is located near the boundary between the Tcr1 or Tcr2 units of the Tiva Canyon formation, which are units forming the caprock along Yucca Crest. The infiltration test was able to consistently maintain applied water fluxes 2 to 3 times greater than the estimated fracture-fill K_{sat} for the caprock. Note that the experimental design may not have limited application rates according to bedrock K_{sat}. Evaporation was limited by placing a tarp on the ground surface, but it is reasonable to expect that some applied water is lost to uptake from laterally extending roots, subsurface evaporation due to air movement, and perhaps lateral redistribution above the bedrock interface. The ability of the bedrock to accept infiltrating fluxes at such large rates strongly suggests that overall bedrock K_{sat} does not limit MAI in the caprock above the potential repository, consistent with the ITYM model.

Waiting, et al. (2001) estimated fracture porosity based on aperture and trace length measurements in three fracture pavements that expose the upper lithophysal unit in the Tiva Canyon formation (the Tcpul unit). Only traces longer than 2 m [6.6 ft] were considered. Each pavement had estimated fracture porosity of approximately 0.006, using segment-by-segment measurements along each fracture trace. Waiting, et al. (2001) estimated an average areal fracture density of 1.93 m/m^2 [0.588 ft/ft^2] for the three pavements, which implies an average fracture aperture of 3.1 mm [0.12 in]. Assuming that the average soil-filled volume fraction is 0.1 for these fractures and the average carbonate-filled volume fraction is 0.7, K_{sat} for the filled fraction is 0.33 mm/d [0.013 in/d]. Based on this calculation, it is likely that fracture porosity at least partially limits MAI for this unit, even if most fractures were filled with soil rather than carbonate and fractures shorter than 2 m [6.6 ft] were included in the estimate, because the maximum K_{sat} for the filled fraction is significantly below the cutoff of 10 mm/d [0.4 in/d] that indicates complete lack of bedrock control on MAI.

DOE measured fracture apertures in a detailed line survey performed in the ESF. Different criteria for mapping traces were used in different sections of the ESF; for consistency in comparison, only sections that mapped fractures with trace lengths greater than 1 m [3.3 ft] are used. The detailed line survey measured the largest and smallest apertures for each trace to the nearest 1 mm [0.04 in]. Almost all minimum apertures were recorded as a zero value. Providing a relative comparison of unit characteristics, Figure 6-17 displays the cumulative distribution of approximate mean fracture aperture within the ESF for lithophysal,

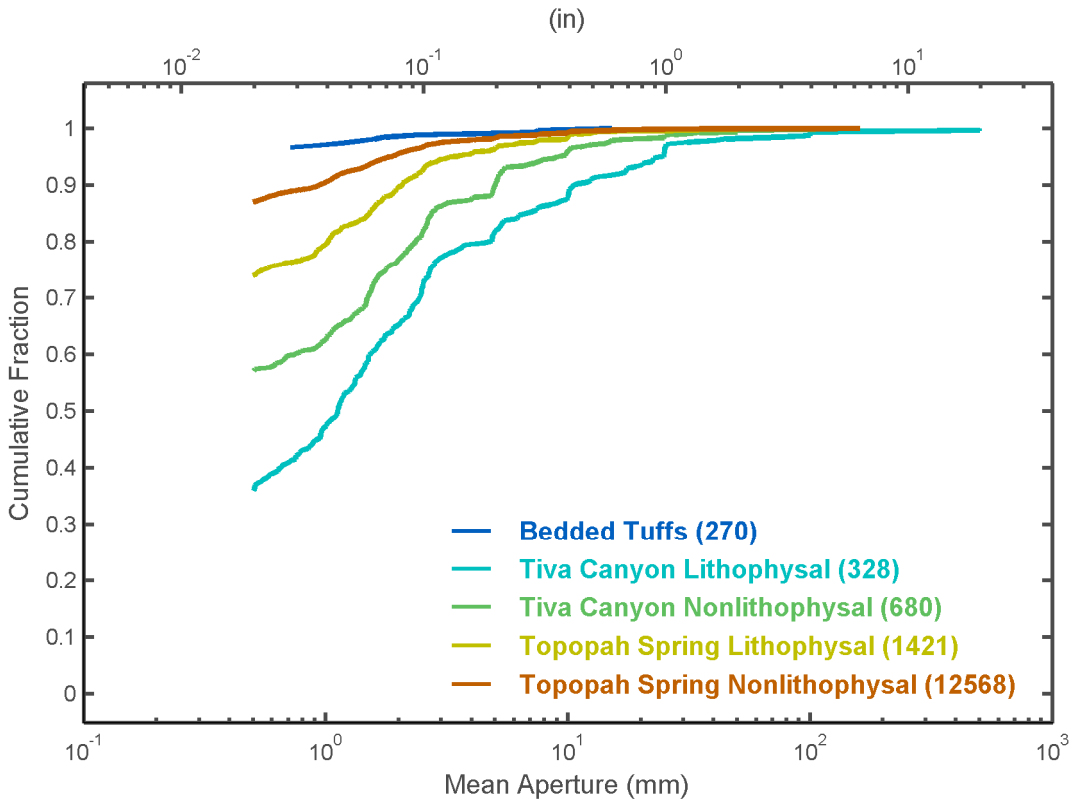

Figure 6-17. Mean Fracture Apertures Observed for the Detailed Line Survey Within the Exploratory Studies Facility. The Mean Aperture Is the Average of the Minimum and Maximum Observed. The Number of Observations Is Indicated in Parentheses.

nonlithophysal, and nonwelded bedded tuff units, using the average of the minimum and maximum recorded apertures to estimate mean aperture. The distributions truncate at the smallest observed nonzero value—the average of 0 and 1 mm [0 and 0.04 in]. The Tiva Canyon units tend to have larger apertures than the Topopah Spring units, which is expected because these units are nearer the ground surface and have little overburden to force fracture closure. The lithophysal units consistently exhibit larger apertures than the nonlithophysal units within the same formation. The nonwelded bedded tuff units have very few observed apertures recorded as nonzero.

The full cumulative distribution of apertures cannot be determined from censored observations, but the distributions are likely to be strongly skewed so that the mean aperture is larger than the median aperture. The median of the fracture apertures from these Tiva Canyon lithophysal units is approximately 1 mm [0.04 in], and the actual mean of this population is likely between 1 and 3 mm [0.04 and 0.12 in]. Assuming that the population mean aperture at depth is 2 mm [0.08 in], comparisons with the pavement calculations suggest that the surface fractures are systematically wider by about 50 percent because of weathering and unloading. The average mapped fracture aperture for the nonlithophysal Tiva Canyon units is approximately 0.5 mm [0.02 in], implying that the mean aperture at the surface is approximately 0.75 mm [0.03 in].

The median fracture separation distance observed in the detailed line survey for fractures with trace length greater than 1 m [3.3 ft] is significantly larger for nonlithophysal units than for lithophysal units. Using summary statistics for fractures greater than 1 m [3.3 ft] in length from

the detailed line survey Smart, et al. (2005, Tables 3-1, 3-3, 3-4, and 3-6) reported, median true spacing for fracture sets 1 and 2 (the predominant subvertical fracture sets) in Tptpul are 6.3 and 0.9 times larger than the corresponding spacing in the intensely fractured zone of Tptpmn (i.e., in the central portion of the Main Drift between ESF stations 42+00 to 51+50), and 2.7 and 1.6 times larger when the intensely fractured zone is excluded. Trace length ratios for these sets are 0.78 and 0.83 (intensely fractured zone) and 0.95 and 1 (excluding the intensely fractured zone).

Fracture volume fraction is directly proportional to the average trace length ratio. Fracture volume fraction is also proportional to the number of fractures per unit length, or the inverse of fracture separation, in both primary directions. Using these scaling arguments with the 1-m [3.3-ft] fracture sets, the fracture volume fraction for the Tptpmn zone is approximately 4.4 to 6.8 times larger than the Tptpul zone and 60 to 94 times larger than the Tptpll zone. Assuming that the fractures are 70 percent soil filled and 20 percent carbonate filled and that average trace-length densities are 6 times larger than the Tcpul unit, the Tcpmn unit has a fracture K_{sat} of approximately 3 mm/d [0.12 in/d]. This value is moderately below the upper cutoff value of 10 mm/d [0. 4 in/d], suggesting that MAI in the Tcpmn may be relatively sensitive to the fracture volume fraction. The fracture properties observed in the detailed line survey are quite spatially variable, so that it is reasonable to infer that the same is true in the analogous units at the surface. As a consequence, it is reasonable to infer that MAI through the Tcpmn zone may be quite spatially variable, perhaps more so than through most of the zones. In a relatively small fraction of the outcrop area the fracture system may not restrict MAI, but MAI may be significantly restricted within the fracture system in a larger fraction of the outcrop area.

The aperture distribution in Figure 6-17 suggests that the mean aperture of nonwelded units may be at least an order of magnitude smaller than the mean aperture for the Tcpmn unit; thus K_{sat} is at least an order of magnitude smaller than for the Tcpmn unit even if the fractures had the same soil-filled fraction and average trace length density. Accordingly, the fracture system in nonwelded tuffs is likely to contribute a negligible amount to MAI.

6.3 Uncertainty in Hydraulic Properties

ITYM describes soil and bedrock using the hydraulic properties of (i) intrinsic permeability, k; (ii) van Genuchten capillary pressure, P_o; (iii) van Genuchten m; and (iv) porosity, ε. ITYM uses the base-10 logarithm of the k, P_o, and ε properties to better describe the correlations between the properties. These properties represent bulk properties at the scale of individual grid cells.

ITYM considers each of the soil and bedrock properties to be variable, with uncertain statistical properties describing the variability. The median values of the ITYM matrix hydraulic properties are identical to corresponding Flint, et al. (1996a) model properties, as described in Sections 6.1 and 6.2, but an independent estimate of parameter uncertainty was developed because the Flint, et al. (1996a) model did not consider uncertainty. The Flint (1998) database of core-sample estimates can be readily used to estimate variability at the scale of individual bedrock core samples, but the magnitude of variability at this scale may not be representative of grid cells. The core samples used to estimate K_{sat} have a cross-sectional area of less than 5 cm^2 [0.8 in^2] and length of 5 cm [2 in], whereas each grid cell has an area of 900 m^2 [9,700 ft^2]. The average hydraulic properties of numerous core samples are less variable than the hydraulic properties of the individual core samples making up the average (a necessary consequence of

averaging) implying that variability at the grid-cell scale is likely to be much smaller than variability at the core-sample scale.

Little field evidence of variability at the grid scale is available from Yucca Mountain, and it is possible that the large upscaling from observation scale to grid scale also enables formation of preferential pathways as a result of local fluctuations, which may result in systematically different effective properties—this potential systematic effect increases the uncertainty in grid-scale parameters. The calibrated properties Bechtel SAIC Company, LLC (2004c) developed, which apply at the scale of entire layers within the three-dimensional unsaturated zone flow and transport model, typically have larger bulk matrix permeability and van Genuchten α relative to the core sample median for the corresponding layers.

The uncertainty in soil, bedrock, and fracture properties used for ITYM simulations is described in Tables 6-1 through 6-3. Tables 6-1 and 6-2 describe the mean values for soil components (Table 6-1) and bedrock components (Table 6-2). Most of the parameters are log transformed; the listed mean values represent the mean of the transformed variable. Table 6-3 describes the variability and uncertainty of the properties about the mean. The ITYM parameter values have not changed since the estimates were developed in 1998.

Three standard deviation values are presented in Table 6-3: spatial variability at the grid scale given a mean estimate (s), uncertainty about the mean estimate (m_u), and uncertainty about the estimate of spatial variability (s_u). The column labeled s_e represents the aggregate standard deviation for the hydraulic property. The aggregate standard deviation is numerically calculated using the formula where δv is the deviation from the mean and the δ values represent noise that is sampled from a zero-mean, unit-variance normal distribution. Values for s_e are estimated using 10^6 realizations of δv. The fifth column represents s_e expressed as a multiplier for properties expressed as the base-10 logarithm.

The same uncertainty property estimates are used for each class (e.g., all soil types use the same uncertainty properties), but sampling is performed independently for each type within a class.

The fine component of the soil within the potential repository footprint is primarily derived from eolian sources and thus appears to have a fairly uniform texture. Limited confirmation field estimates of K_{sat} are in good agreement with estimates from pedotransfer functions using soil texture. For these reasons, both soil hydraulic conductivity and soil porosity are assigned rather low uncertainty and low variability. However, data is lacking regarding soil retention properties; thus P_o is considered quite uncertain. The assigned uncertainty parameters for P_o and m yield aggregate uncertainty in $\log_{10}(P_o)$ and m of 0.71 and 0.07, respectively. Assigned uncertainties for m do not affect MAI, because MAI is insensitive to m in the range estimated for Yucca Mountain soil.

CRWMS M&O (2003) considered uncertainty in both soil and bedrock K_{sat}, describing both as lognormally distributed with a standard deviation of 0.4 for $\log_{10}(K_{sat})$ based on the literature. The same standard deviation would apply for $\log_{10}(k)$, because K_{sat} is obtained by multiplying k by a constant factor. The models DOE uses to estimate infiltration [e.g., INFIL, Mass Accounting System for Soil Infiltration and Flow (MASSIF)] do not consider retention properties for either soil or bedrock.

Table 6-1. Mean Parameter Values for Soil Hydraulic Properties*						
Soil or Soil Component	**$\log_{10}(k)$†**	**$\log_{10}(P_o)$‡**	**m§**	**$\log_{10}(\varepsilon)$‖**	**$\log_{10}(f_{ss})$¶**	**$\log_{10}(f_{sr})$#**
Typic Argidurids	–8.243	0.2840	0.1935	–0.4365	–0.04818	–0.9788
Typic Haplocalcids	–7.912	0.2076	0.2366	–0.5017	–0.05355	–0.9355
Typic Haplocambids	–7.877	0.1805	0.2647	–0.4881	–0.08991	–0.7282
Typic Torriorthents	–7.411	0.06048	0.3827	–0.5513	–0.1073	–0.6596
Lithic Haplocambids	–8.165	0.2518	0.4382	–0.4815	–0.0716	–0.8182
Typic Torripsamments	–7.560	0.1308	0.2857	–0.4698	–0.05404	–0.9318
Lithic Haplargids	–8.243	0.2596	0.2063	–0.4318	–0.08145	–0.7670
Rock	–8.165	0.2518	0.4382	–0.4815	–0.1549	–0.5229
Typic Calciargids	–8.235	0.2596	0.2308	–0.4921	–0.09205	–0.7190
Rock Fragments	–11.99	1.301	0.2308	–1		

*Nomenclature for soil follows Flint, A.L., J.A. Hevesi, and L.E. Flint. "Conceptual and Numerical Model of Infiltration for the Yucca Mountain Area, Nevada." Milestone 3GUI623M. Las Vegas, Nevada: Department of Energy. 1996.
†k = intrinsic permeability [cm^2]
‡P_o = van Genuchten pressure [kPa]
§m = van Genuchten m
‖ε = porosity
¶f_{ss} = soil volume fraction
#f_{sr} = rock volume fraction

Table 6-2. Mean Parameter Values For Bedrock Hydraulic Properties*							
Hydrogeologic Unit or Fracture Fill Type	**$\log_{10}(k)$†**	**$\log_{10}(P_o)$‡**	**m§**	**$\log_{10}(\varepsilon)$‖**	**$\log_{10}(f_{fc})$¶**	**$\log_{10}(f_{fs})$#**	**$\log_{10}(f_{fu})$****
Qtac	–13.23	2.907	0.4083	–1.143	–4.983	–6.886	–5.607
Qtc	–13.23	2.907	0.4083	–1.143	–4.983	–6.886	–5.607
CNW	–9.269	1.616	0.2754	–0.4522	–4.995	–6.472	–4.634
TC	–11.79	2.053	0.1994	–1.420	–6.377	–4.382	–7.377
CUC	–10.41	2.082	0.4565	–0.6144	–3.000	–1.005	–4.000
CUL	–10.89	1.853	0.3460	–0.8125	–4.639	–5.484	–5.183
TMN	–8.386	0.7474	0.1890	–0.4034	–4.269	–3.725	–4.570
TCW	–13.23	2.907	0.4083	–1.143	–4.605	–5.450	–5.149
BT4	–8.386	0.7474	0.1890	–0.4034	–5.055	–5.055	–4.930
BT3	–9.272	0.3815	0.1896	–0.4737	–5.065	–5.065	–4.940
TPP	–9.049	0.3978	0.3307	–0.3478	–5.085	–5.085	–4.960
BT2	–8.365	0.2787	0.2175	–0.3565	–5.088	–5.088	–4.963
TR	–11.77	1.423	0.5832	–0.8356	–6.466	–4.471	–7.466
TUL	–12.70	2.182	0.2487	–0.8416	–4.639	–5.484	–5.183
TLL	–12.63	2.564	0.2272	–0.9208	–4.542	–5.387	–5.086
Carbonate fill	–9.939	2.000	0.5000	–0.3979			
Soil fill	–7.903	0.1139	0.3450	–0.3279			
Unfilled	4.939	–2.009	0.7000	0			

*Nomenclature for soil follows Flint, A.L., J.A. Hevesi, and L.E. Flint. "Conceptual and Numerical Model of Infiltration for the Yucca Mountain Area, Nevada." Milestone 3GUI623M. Las Vegas, Nevada: Department of Energy. 1996.
†k = intrinsic permeability [cm^2]
‡P_o = van Genuchten pressure [kPa]
§m = van Genuchten m
‖ε = porosity
¶f_{fc} = carbonate-filled fracture volume fraction
#f_{fs} = soil-filled fracture volume fraction
**f_{fu} = unfilled-fracture volume fraction

Table 6-3. Description of Variability and Uncertainty in Hydraulic Properties					
Hydraulic Property	***s****	***m_u*†**	***s_u*‡**	***s_e*§**	***s_e* as Multiplier**
Soil and Bedrock Properties					
log(*k*)‖	0.1	0.1	0.05	0.150	1.412
log(P_o)¶	0.5	0.5	0.05	0.709	5.116
m#	0.05	0.05	0.01	0.071	
log(ε)**	0.05	0.05	0.01	0.071	1.179
Carbonate Fill in Fractures					
log(*k*)	2	2	0.5	2.830	676.41
log(P_o)	1	0.5	0.1	1.123	13.27
m	0.05	0.05	0.01	0.071	
log(ε)	0.05	0.05	0.01	0.072	1.18
Soil Fill in Fractures					
log(*k*)	0.5	0.1	0.05	0.513	3.25
log(P_o)	0.5	0.5	0.05	0.714	5.18
m	0.05	0.05	0.01	0.071	
log(ε)	0.05	0.05	0.01	0.071	1.18
Unfilled Fractures					
log(*k*)	0.5	1	0.1	1.123	13.27
log(P_o)	0.5	1	0.05	1.120	13.17
m	0.05	0.01	0.01	0.071	
log(ε)	0	0	0	0.000	1.00
Soil Mixture					
$\log_{10}(f_{sr})$††	0.1	0.1	0.1	0.173	1.49
Bedrock Mixture					
$\log_{10}(f_{fc})$‡‡	0.1	0.1	0.1	0.173	1.49
$\log_{10}(f_{fs})$§§	0.1	0.1	0.1	0.173	1.49
$\log_{10}(f_{fu})$‖‖	0.1	0.1	0.1	0.173	1.49

*s = standard deviation describing variability
†m_u = standard deviation describing uncertainty in the mean value
‡s_u = standard deviation describing uncertainty in the standard deviation
§s_e = standard deviation describing cumulative variability and uncertainty
‖k = intrinsic permeability [cm^2]
¶P_o = van Genuchten pressure [kPa]
#m = van Genuchten m
**ε = porosity
††f_{sr} = rock volume fraction
‡‡f_{fc} = carbonate-filled fracture volume fraction
§§f_{fs} = soil-filled fracture volume fraction
‖‖f_{fu} = unfilled-fracture volume fraction

The ROSETTA program for estimating soil hydraulic parameters using pedotransfer functions has a large database of hydraulic measurements. Ridgetop and hillslope soil texture ranges from loamy sand to loam, based on limited confirmatoion analyses of sand, silt, and clay fractions within the potential repository footprint (Stothoff, et al., 1999). Schaap and Leij (1998)

report class-average values within the ROSETTA database that have a standard deviation range of (i) 0.64 to 0.92 for $\log_{10}(K_{sat})$ using 594 measurements and (ii) 0.47 to 0.73 for $\log_{10}(P_o)$ using 935 measurements in the loamy sand, sandy loam, and loam classes that are typical of Yucca Mountain soil. The ROSETTA values suggest that the assigned ITYM uncertainties are quite low for soil K_{sat} and on the high end of the range for P_o. The ROSETTA values represent a significantly smaller scale than the grid cells used in ITYM so that values on the ITYM grid scale would tend to have lower variability. On the other hand, features such as macropores and textural alteration due to carbonates within the soil are not included in the abstraction, making the appropriate value for P_o more uncertain. The uncertainty values used by ITYM to describe P_o balance these considerations.

The representation of uncertainty used to describe soil parameters is also used to describe bedrock parameters. Direct measurement (Flint, 1998) provides numerous values for hydraulic properties of core samples, which (like the soil core samples) have a cross-sectional area more than six orders of magnitude smaller than a grid cell, causing similar difficulties with regard to upscaling. Further, the core samples described by Flint (1998) were obtained at depth from boreholes, and properties near the soil/bedrock interface may be systematically different due to weathering. In retrospect, intrinsic permeability values in bedrock are likely more uncertain than in soil and more uncertain than considered by ITYM. However, ITYM estimates of MAI may not be very sensitive to uncertainty in intrinsic permeability, because either the fracture system dominates the bedrock in determining MAI or bedrock permeability is too small to permit significant MAI for most of the domain

$$\delta v = m_u \delta_1 + (s + s_u \delta_2)\delta_3 \tag{6-2}$$

ITYM uses equivalent or larger values, relative to the soil and bedrock values, to represent uncertainty in fracture-class hydraulic properties. The range of K_{sat} measurements shown in Figure 6-11 spans approximately eight orders of magnitude; thus carbonate fracture fill is assigned a rather large uncertainty for $\log_{10}(k)$. The uncertainty in P_o is somewhat larger than for soil or bedrock. The uncertainty in $\log_{10}(k)$ for soil fill is considered larger than the uncertainty in the overlying soil, because the texture of the soil fill may be different than the overlying soil if differential movement of different particle sizes occurs or if the texture is somewhat altered by carbonate precipitation. ITYM also uses large uncertainty values for unfilled-fracture $\log_{10}(k)$ and $\log_{10}(P_o)$. Uncertainty in m and ε is assumed to be the same as for soil and bedrock (except for unfilled fractures, where it is certain that $\varepsilon = 1$).
The columns in Table 6-4 represent the correlation matrix used for sampling hydraulic properties for each soil, bedrock, and fracture type. Correlations between properties are based on staff experience that suggests $\log_{10}(k)$ is somewhat negatively correlated with $\log_{10}(P_o)$ and somewhat more strongly positively correlated with $\log_{10}(\varepsilon)$. ITYM uses a slightly weaker negative correlation between $\log_{10}(P_o)$ and $\log_{10}(\varepsilon)$ to be consistent with the correlations involving k. Correlations between m and other properties are set to zero, because the abstractions for MAI are essentially insensitive to m, even though van Genuchten m is likely correlated with other hydraulic properties.

All off-diagonal correlation coefficients are assigned a standard deviation of 0.2 to account for uncertainty in the actual value of the coefficient. Correlation coefficients falling outside the range of −1 to 1 during sampling are resampled until the bounds are satisfied.

Table 6-4. Correlation Coefficient Matrices Between Properties for Hydraulic Properties				
Soil and Rock Properties	**$\log_{10}(k)$***	**$\log_{10}(P_o)$†**	***m*‡**	**$\log_{10}(\varepsilon)$§**
$\log_{10}(k)$	1	−0.6	0	0.7
$\log_{10}(P_o)$	−0.6	1	0	−0.5
m	0	0	1	0
$\log_{10}(\varepsilon)$	0.7	−0.5	0	1
Soil Mixture	**$\log_{10}(f_{ss})$‖**	**$\log_{10}(f_{sr})$¶**		
$\log_{10}(f_{ss})$	1	−1		
$\log_{10}(f_{sr})$	−1	1		
Bedrock Mixture	**$\log_{10}(f_{ft})$#**	**$\log_{10}(f_{fc})$****	**$\log_{10}(f_{fs})$††**	**$\log_{10}(f_{fu})$‡‡**
$\log_{10}(f_{ft})$	1	−1	−1	−1
$\log_{10}(f_{fc})$	−1	1	0	0
$\log_{10}(f_{fs})$	−1	0	1	0
$\log_{10}(f_{fu})$	−1	0	0	1

*k = intrinsic permeability [cm^2]
†P_o = van Genuchten pressure [kPa]
‡m = van Genuchten m
§ε = porosity
‖f_{ss} = soil volume fraction
¶f_{sr} = rock fragment volume fraction
#f_{ft} = bedrock matrix volume fraction
**f_{fc} = carbonate-filled fracture volume fraction
††f_{fs} = soil-filled fracture volume fraction
‡‡f_{fu} = unfilled-fracture volume fraction

6.4 Summary

The ITYM model considers two abstractions describing the influence of soil and bedrock on MAI: an abstraction for deep soil and an abstraction for shallow soil overlying bedrock. Most of the area near the potential repository is thought to have a soil thickness less than 1 m [3.3 ft], which is handled with the shallow-soil abstraction. The shallow-soil abstraction considers the effect on MAI from both the bedrock matrix and the fracture system; the deep-soil abstraction does not consider bedrock.

Both abstractions consider soil hydraulic properties as well as the effect of rock fragments within the soil matrix on reducing MAI. Most of the area ITYM considered consists of (i) surficial deposits with an unaltered or mildly altered eolian-derived fine matrix with various proportions of embedded clasts or (ii) alluvial/colluvial deposits that are interpreted to have been deposited subsequent to the last glacial maximum. Older deposits are limited to areas with deep soil and are generally not found within the potential repository footprint. ITYM follows the aggregation scheme Flint, et al. (1996a) derived for the soil maps Lundstrom, et al. (1996, 1995, 1994) and Lundstrom and Taylor (1995) developed. Soil hydraulic properties are considered uncertain, with values Flint, et al. (1996a) derived used as the median value in the ITYM distribution but with independent estimates of uncertainty.

The shallow-soil abstraction considers four pathways for infiltration into the bedrock: (i) bedrock matrix or (ii) soil-filled, (iii) carbonate-filled, and (iv) unfilled fractures. Each pathway has an

associated volume fraction. Separate calculations to estimate MAI are made for each pathway in each grid cell; the pathway with the largest estimated MAI is used for the grid cell. With this approach, hydraulic properties are needed for each pathway, as well as the volume fraction for the pathway. ITYM follows the aggregation scheme Flint, et al. (1996a) derived for the bedrock map Day, et al. (1998) developed. Bedrock and fracture hydraulic properties are considered uncertain, with values Flint, et al. (1996a) derived providing a basis for the median value in the ITYM distribution where available but with independent estimates of uncertainty. The volume fraction for each pathway is also based on estimates Flint, et al. (1996a) derived for most units, but independent estimates are used for caprock units.

Bulk hydraulic properties are considered a separate class for each soil unit and bedrock pathway. Saturated hydraulic conductivity, the two van Genuchten retention parameters, and porosity are sampled as correlated parameters for each class. Volume fractions are also considered correlated parameters for the soil and bedrock unit, with the constraint that volume fractions must sum to one.

Independent confirmatory analyses suggest that the hydraulic properties ITYM used are generally reasonable even though additional information suggests modifications to some of the parameter values. The confirmation analyses suggest that alternative median fracture volume fraction estimates for the Tcpmn and Tcpul units may lead to higher estimates for MAI above the potential repository footprint. ITYM does estimate nonzero expected MAI in these units, however, because (i) the property values are not well known, (ii) ITYM considers the properties to be quite uncertain, and (iii) model-estimated MAI is quite sensitive to the particular values of these properties. These assumptions lead to occasional realizations with large MAI, implying that expected MAI is nonzero.

7 SITE-SPECIFIC SOIL THICKNESS

The abstractions developed in Section 4 are sensitive to the hydraulic properties and thickness of the overlying surficial material in areas with shallow soil cover. Section 6 discussed the mapped spatial patterns of the surficial deposits and associated hydraulic properties of the soil. A detailed map of present-day shallow soil thickness is not available, and soil thickness may be difficult to measure in a noninvasive manner at the scale of several watersheds. A numerical approach to estimating soil thickness is presented in Section 7, using a mechanistic equilibrium soil mass-balance model. The model is used as a preprocessor to the Infiltration Tabulator for Yucca Mountain (ITYM).[1] The model considers dust deposition, bedrock weathering, sediment transport, and downhill creep to estimate soil thickness, using a digital elevation model (DEM)[2] for the underlying elevation controls. The same DEM underlying the ITYM model is used to produce soil-thickness input for ITYM. ITYM internally multiplies the soil thickness in all grid cells by a single sampled parameter for each realization of input parameter values to consider the effect on mean annual infiltration (MAI)[3] resulting from uncertainty in the soil-thickness distribution.

The equilibrium model describes present-day conditions assuming that the underlying processes are in approximate equilibrium. The cu, cs, and rc surficial deposits indicated in Figure 6-1 are most likely to satisfy this assumption, because these units probably predominantly reflect conditions existing since the end of the last glacial maximum, and these surficial deposits cover most of the ground surface above the repository footprint. The equilibrium assumption is a useful simplification of the current understanding of the processes, enabling rapid calculation of soil profiles.

Section 7.1 describes the conceptual and mathematical underpinnings of the model in some detail, with the numerical approach used to solve the mathematical model presented in Section 7.2. Section 7.3 presents the soil depth distribution used in ITYM, using a 30-m [98-ft] grid with elevations derived from a standard U.S. Geological Survey DEM, and compares the ITYM distribution to subsequently developed confirmatory simulations using a 7.5-m [25-ft] grid. Section 7.4 illustrates the sensitivity of the soil-thickness model to grid dimensions and model input parameters in an approximately 1.5 km^2 [0.6 mi^2] rectangle including the upper Split Wash watershed and parts of the west flank of Yucca Mountain and Yucca Crest, considering grids between 7.5 m [25 ft] and 1.9 m [6.2 ft] on a side. Section 7.5 considers implications of different climatic regimes on soil thickness and the resulting effect on MAI. Finally, Section 7.6 summarizes important information from Section 7.

7.1 Soil-Balance Processes

Feedback cycles affecting soil thickness and texture are shown schematically in Figure 7-1. Climate drives the overall process. Effective moisture, a qualitative term describing the

---

[1] Infiltration Tabulator for Yucca Mountain is used frequently throughout this chapter; consequently, the abbreviation ITYM will be used.

[2] Digital elevation model is used frequently throughout this chapter; consequently, the abbreviation DEM will be used.

[3] Mean annual infiltration is used frequently throughout this chapter; consequently, the abbreviation MAI will be used.

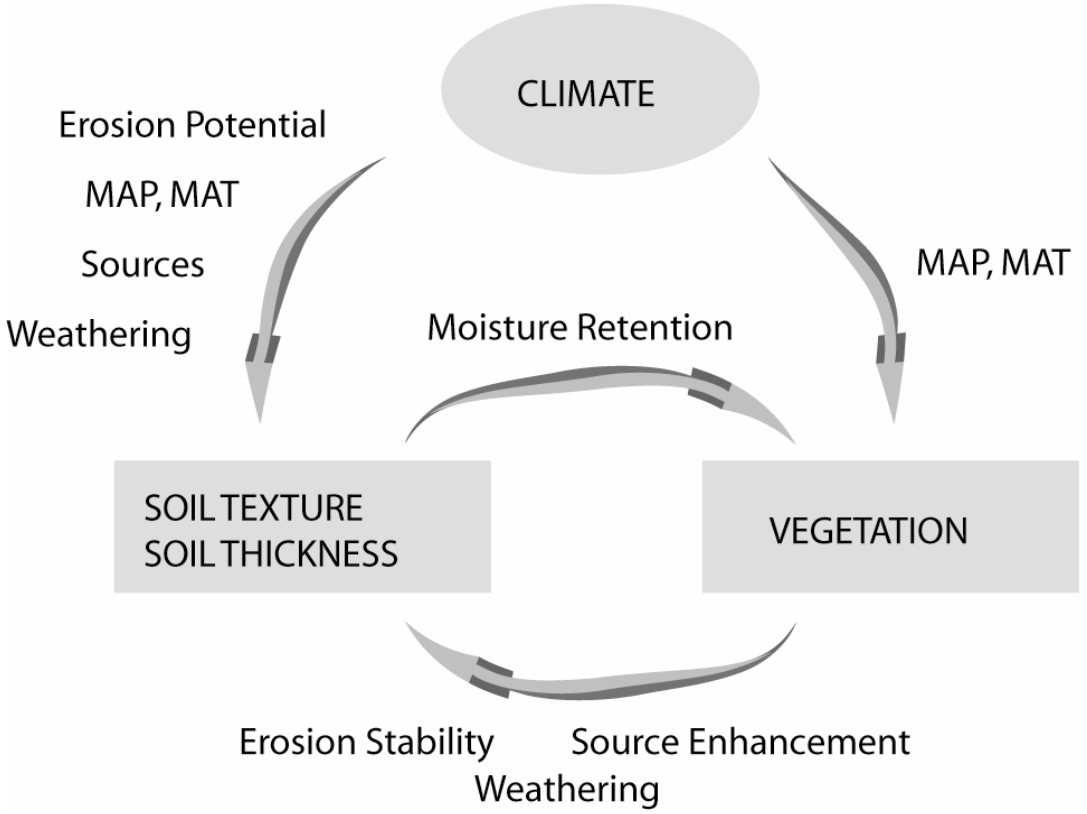

Figure 7-1. Conceptual Representation of Major Influences on Soil Characteristics

combined influences of mean annual precipitation (MAP)[4] and mean annual temperature (MAT)[5] on soil moisture, directly affects vegetation. Effective moisture also affects erosion potential, weathering rates, and atmospheric dust sources. Feedback between vegetation and soil thickness and texture also occurs.

These conceptual processes must be quantified in a series of mathematical formulas that can be linked in a computational model to predict soil characteristics under present and future climatic conditions. The processes include

- Atmospheric interactions including deposition and removal of fine particles
- Soil transport of particles through overland flow (runoff, rainsplash)
- Bulk movement of soil through creep and slump
- *In situ* mechanical weathering
- Chemical weathering
- Entrainment of particles from the bedrock

[4] Mean annual precipitation is used frequently throughout this chapter; consequently, the abbreviation MAP will be used.

[5] Mean annual temperature is used frequently throughout this chapter; consequently, the abbreviation MAT will be used.

Each of these processes is discussed in this section, with simple mathematical representations proposed.

7.1.1 Atmospheric Interactions

Dust is the primary source of fine particles under current climatic conditions. Dust is eroded from relatively local sources such as dry playas and deposited over a wide area. When deposition occurs near the source, changes in the local source may need to be considered over the period of interest. There appears to be no dominant dust source near Yucca Mountain, so it is reasonable to consider regional changes in atmospheric dust concentrations and dust deposition rates.

Reheis, et al. (1995) estimated paleo and present-day dust deposition rates in the Yucca Mountain region, including sites at Fortymile Wash and Yucca Wash. Reheis, et al. (1995) examined dust deposition rates for the last 15,000 years in southern Nevada estimating approximately 6, 3, and 2 $g/m^2/yr$ [0.02, 0.001, and 0.0066 $oz/ft^2/yr$] for silt, clay, and $CaCO_3$, respectively, for a total accumulation rate of approximately 11 $g/m^2/yr$ [0.036 $oz/ft^2/yr$]. Extreme values reported by Reheis, et al. (1995) for each category would yield peak rates of no more than 65 $g/m^2/yr$ [0.21 $oz/ft^2/yr$]. The fine component of Yucca Mountain soil consists of approximately 67 percent sand, 25 percent silt, and 7 percent clay, implying that total dust deposition rates, including sand, are approximately 33 $g/m^2/yr$ [0.11 oz/ft^2yr]. With a representative porosity of 0.4 and particle density of 2.5 g/cm^3 [56 lb/ft^3] a deposition rate of 33 $g/m^2/yr$ [0.11 07/ft^2yr] implies that, on average, soil thickness is increasing at a rate of approximately 22 cm [3.7 in] per 10,000 years.

Current understanding of hillslope soil dynamics in the arid southwest suggests that soil profiles gradually deepened and developed a finer texture over the last glacial cycle, and then hillslopes were largely stripped of soil once the climate dried sufficiently to reduce plant densities below a critical level some time after the last glacial maximum (Bull, 1991). As discussed in Section 6.1, Lundstrom, et al. (1996, 1995, 1994) and Lundstrom and Taylor (1995) mapped several surficial deposit units in the washes that are dated as Holocene and late Pleistocene, consistent with this current understanding. The assumption that the deepest eolian soil found on Yucca Crest, roughly 50 cm [20 in] thick, was deposited in the last 10,000 years yields a maximum dust deposition rate on the order of 4 cm/ky [1.6 in/ky] if the soil includes 20 percent rock fragments. Typical soil thicknesses are 20–30 cm [8–12 in], consistent with the estimate using the Reheis, et al. (1995) dust deposition rates. Dust deposition rates on sideslopes may be systematically larger than on the exposed crest, because washes are sheltered from the wind. Confirmatory deposition-rate estimates are difficult for hillslopes because they are far steeper than the relatively horizontal caprock, with much more erosive overland flow and enhanced downhill transport due to rain splash, so deposited dust is more likely to be removed downslope. As a first approximation, spatial variability of dust deposition is neglected in the computational model. Because estimates of dust deposition rates appear to be reasonably consistent with observations at Yucca Mountain, the spatially uniform dust deposition rates in the model are constrained to be consistent with rates estimated by Reheis, et al. (1995).

7.1.2 Soil Transport Through Overland Flow

Transport of soil particles through overland flow moves particles from higher elevations to lower elevations via flowing water. For a given storm, the approach advocated by Flanagan and Nearing (1995) is straightforward. In this approach, sediment transport is modeled using equivalent steady-state water flows. Flanagan and Nearing (1995) obtain the equivalent steady

state from transient simulations, using the maximum flux within each cell as the flux for the cell. An equivalent period of flux is obtained by dividing cumulative discharge over the storm by the maximum flux. These equivalent steady fluxes are used for erosion and deposition calculations.

Erosion and deposition through overland flow can be calculated using a steady sediment-balance equation

$$\nabla \cdot c_s q_w - Q_{\text{str}} = 0 \tag{7-1}$$

where

c_s — concentration of the sediment in water [M/L^3]
q_w — volumetric water flux vector [L^3/L^{2}T]
Q_{str} — sediment transfer flux between streambed and water column [M/L^{2}T]

Following standard practices in the literature (e.g., Woolhiser, et al., 1990), a kinetic rate law is used to characterize erosion and deposition

$$Q_{str} = C_g \left(c_s - c_{eq} \right) \tag{7-2}$$

where c_{eq} is the equilibrium sediment concentration [M/L^3] for a reach along a streambed and C_g is an equilibrium rate constant [L/T].

Numerous equilibrium sediment concentration capacity relationships exist in the literature (e.g., Yang, 1973; Kilinc and Richardson, 1973; Ackers and White, 1973; Yalin, 1963). A particularly simple relationship is used herein (Meyer and Wischmeier, 1969), based on tractive force

$$c_{eq} = C_s \frac{v^4}{h} \tag{7-3}$$

where

C_s — proportionality constant [MT^4/L^6]
v — water speed [L/T]
h — hydraulic depth [L]

During erosion (i.e., $c_s < c_{eq}$), C_g is a constant describing the erodibility of the alluvium or bedrock. During deposition (i.e., $c_s > c_{eq}$), C_g is estimated with the assumption that the sediment particles have fall velocities and drag characteristics similar to spheres (Fair and Geyer, 1954), with a coupled set of equations used to calculate C_g

$$v_s = \left(\frac{4}{3} \frac{\rho_s - \rho_f}{\rho_f} \frac{g d_s}{C_D} \right)^{1/2} \tag{7-4}$$

$$C_D = \frac{24}{\text{Re}} + \frac{3}{\sqrt{\text{Re}}} + 0.34 \tag{7-5}$$

$$Re = \frac{v_s d_s \rho_s}{\mu} \tag{7-6}$$

$$C_g = \frac{v_s}{h}\left(1 - \frac{c_{eq}}{c_s}\right) \tag{7-7}$$

where

v_s	—	particle settling velocity [L/T]
ρ_s	—	soil density [M/L^3]
ρ_f	—	water density [M/L^3]
g	—	acceleration due to gravity [L/T^2]
d_s	—	particle diameter [L]
C_D	—	drag coefficient [—]
Re	—	reynolds number [—]
μ	—	fluid viscosity [M/LT]

An equivalent steady-state water-balance equation is used to provide the flux of water used for sediment transport

$$\nabla \cdot q_w - Q_{\text{rain}} = 0 \tag{7-8}$$

where Q_{rain} is the net rainfall minus net infiltration. A standard practice in the literature is to use a kinematic-wave approximation for hydraulic flux in conjunction with the Manning hydraulic resistance law so that (in metric units)

$$q_w = \frac{S^{1/2} h^{5/3}}{n} \tag{7-9}$$

where S is the hydraulic slope and n is the Manning roughness coefficient. The kinematic-wave approach requires that each cell has an outlet.

7.1.3 Bulk Movement of Soil

Gravity has a tendency to move soil masses downslope through creep and slump. Creep is slow bulk movement of the soil profile through accumulated small movements, while slump is sudden failure of the soil mass resulting in fast bulk movement. Creep is facilitated through processes that rearrange soil particles, such as freeze–thaw cycles or seismic events, and is dependent on soil texture. Creep may occur through the entire soil profile; surficial processes such as rainsplash enhance downhill movement near the ground surface. Slump also depends on soil texture, but generally occurs when the soil column is extremely moist or as a consequence of large seismic events. Slump rarely occurs under present-day conditions at Yucca Mountain, although in 1984 a slow-moving, localized, intense summer rainstorm stripped 7,040 m^3 [5.7 acre-ft] of soil from Jake Ridge, about 6 km [3.7 mi] east of Yucca Crest (TRW Environmental Safety Systems, Inc., 1998). TRW Environmental Safety Systems, Inc. (1998) estimates that the recurrence rate of such incidences is at least 500 years based on the thickness of existing soil profiles. Although a less dramatic form of mass wasting, creep often occurs in the same environments and mediates the refilling of slump reservoirs (Sidle, et al., 1985).

The soil-thickness computational model uses a film-flow approximation to mass wasting. For a viscous film on an incline (Bird, et al., 1960)

$$v = \frac{\rho g b^2 \cos\beta}{2\mu}\left[1 - \left(\frac{x}{b}\right)^2\right] \tag{7-10}$$

$$\bar{v} = \frac{\rho g b^2 \cos\beta}{3\mu} \tag{7-11}$$

$$q = \frac{\rho g b^3 \cos\beta}{3\mu} \tag{7-12}$$

where

v	—	velocity tangential to the incline [L/T]
$\bar{v}$	—	depth-averaged velocity tangential to the incline [L/T]
q	—	volumetric flux tangential to the incline per unit width [L^3/LT]
ρ	—	bulk density [M/L^3]
b	—	layer thickness [L]
μ	—	layer viscosity [M/LT]
x	—	distance below the top of the layer [L]

Typical viscosity values for earth materials are shown in Table 7-1.

Soils are sometimes considered Bingham materials to estimate slope failure. Bingham materials require a yield stress to be exceeded before deformation occurs as a fluid with constant viscosity. The Bingham model neglects the response of soils to shear stresses below the yield stress, although slow creeping movements generally do occur at these lower stresses. Measured Bingham yield stress and viscosity strongly depend on moisture content and texture (Ghezzehei and Or, 2000), implying that yield strength and viscosity may both change by several orders of magnitude over the range of environmental conditions experienced in a typical decade. By implication, the soil viscosity used in evaluating downhill movement also may vary by several orders of magnitude, with viscosity decreasing as soil water content increases.

7.1.4 Mechanical Weathering

Weathering can be mechanical or chemical in nature. Mechanical processes tend to operate preferentially on larger particles, as the number of potential fracture planes is proportional to volume. On the other hand, chemical processes are most important on particle surfaces (see Section 7.1.5) and thus are most important on small particles with large surface-area-to-volume ratios.

Table 7-1. Dynamic Viscosity for Typical Earth Materials*	
Material	**Dynamic Viscosity (N·s/m^2)**
Mantle	10^{20}
Shale	10^{16}
Evaporites	10^{13} to 10^{16}
Glacier ice	10^{12} to 10^{13}
Magma	10^{2} to 10^{3}
Flowing lava	10^{1} to 10^{2}
Debris flows	7.5×10^{2}
Mudflows	2×10^{2} to 6×10^{2}
Solifluction	10^{2}
Water at 20 °C	10^{-3}
*Selby, M.J. *Hillslope Materials and Processes*. 2nd Edition. Oxford, England: Oxford University Press. 1993.	

Mechanical weathering arises when stresses in the rock are great enough to rupture the rock. Ruptures can occur along fracture planes or grain boundaries. The processes most commonly reported as causing mechanical weathering include expansion during freezing or salt crystallization, unloading after erosion, and expansion and contraction during thermal loads such as diurnal fluctuations or fire (Birkeland, 1999).

Relative freeze–thaw activity can be quantified. For freeze–thaw cycling to be effective, soil temperatures must cycle across the freezing point so that water can repeatedly freeze and melt (and liquid water must be present to freeze). The number of times the freezing point is crossed during a year is a measure of the relative importance of freeze–thaw activity on mechanical weathering.

The expected fraction of days in a year with a freeze–thaw cycle can be calculated given mean seasonal and diurnal temperature variation, the variance of the daily mean temperature about the seasonal mean, and the variance of the daily temperature range. This information is sufficient to generate numerous realizations of daily maximum and minimum temperatures for each day of the year in a Monte Carlo simulation. A freeze–thaw cycle occurs if the minimum and maximum temperatures are on opposite sides of the freezing temperature.

If the two variance variables are assumed normal and correlated, realizations may be generated by first sampling one and then creating the other from the first using

$$m_{Y|X} = m_Y + \rho \frac{\sigma_Y}{\sigma_X}\left(x - m_X\right) \tag{7-13}$$

$$\sigma^2_{Y|X} = \left(1 - \rho^2\right)\sigma^2_Y \tag{7-14}$$

where m represents the mean, σ^2 is the variance, and ρ is the correlation coefficient (Benjamin and Cornell, 1970).

With no correlation between the variance variables, the number of days with a freeze–thaw cycle is bell shaped as a function of mean daily temperature and has a peak centered on 0 °C [32 °F]. A positive correlation shifts the temperature at the peak below 0 °C [32 °F], with statistical parameters typical of natural climates causing a shift on the order of a degree. Direct simulation suggests that the fraction of days having a freeze–thaw cycle is proportional to the standard deviation of the range in daily temperature and inversely proportional to the standard deviation for the daily average deviation. Halving the standard deviation of the daily temperature range halves the fraction of days with freeze–thaw cycles. Doubling the standard deviation for the daily average deviation also halves the fraction of days with freeze–thaw cycles, but doubles the spread of the curve and doubles the shift due to the correlation coefficient.

Temperature perturbations decay with depth into the soil column, shrinking both standard deviations equally. The net effect would be to keep the same peak but decrease the spread of the curve.

The daily minimum and maximum temperatures for nearby Beatty, Nevada, over the period from 1948 through 1994 (with several missing intervals), were used to estimate typical statistical parameters. The difference between maximum and minimum temperature varies slightly over the year, with the mean difference (all temperatures in Celsius) having the relationship

$$\overline{\Delta} = 18.3727 + 2.7465 \sin\left[2\pi(J - 113.24)/365.25\right] \tag{7-15}$$

where $\overline{\Delta}$ is the mean difference and J is the Julian day of the year. The observed deviation from the mean is slightly skewed, with a mean of −0.56 °C [−1.01 °F] and a standard deviation of 4 °C [7.2 °F].

The seasonal mean temperature T (the mean of maximum and minimum) is also approximately sinusoidal

$$T = 15.5 + 10.8 \sin\left[2\pi\left(J - 112\right)/365.25\right] \tag{7-16}$$

A histogram of the observed deviation from T is less skewed than the histogram for $\overline{\Delta}$, with a mean of −0.18 °C [−0.32 °F] and a standard deviation of 3.62 °C [6.52 °F]. The correlation between daily-mean deviation and temperature-range deviation is 0.241. From this information, assuming normality for both distributions allows calculation of the number of freeze–thaw days and the fraction of time spent at various temperatures over the course of a year.

It is assumed that the decay of the temperature amplitude with depth can be applied to the standard deviations for daily temperature range and daily-mean deviation. Thus, both standard deviations are multiplied by $\exp(-z/D)$, where z is depth below the soil surface, characteristic decay depth $D = (2\ k_h/\omega\ C_h)^{1/2}$, and $\omega = 2\pi/24$ (representing a daily cycle). With typical soil thermal properties, D for daily perturbations is approximately 15 cm [6 in].

Typical cases are shown in Figure 7-2, using the standard deviations, correlation coefficient, amplitudes, and offsets determined using the Beatty data set and using 10^6 realizations for each day. Only MAT and depth are varied. The peaks in Figure 7-2 correspond to the cases where the peak of either summer or winter has an expected temperature of 0 °C [32 °F]. The decay of the amplitude of the annual cycle with depth is also considered, tending to bring the peaks

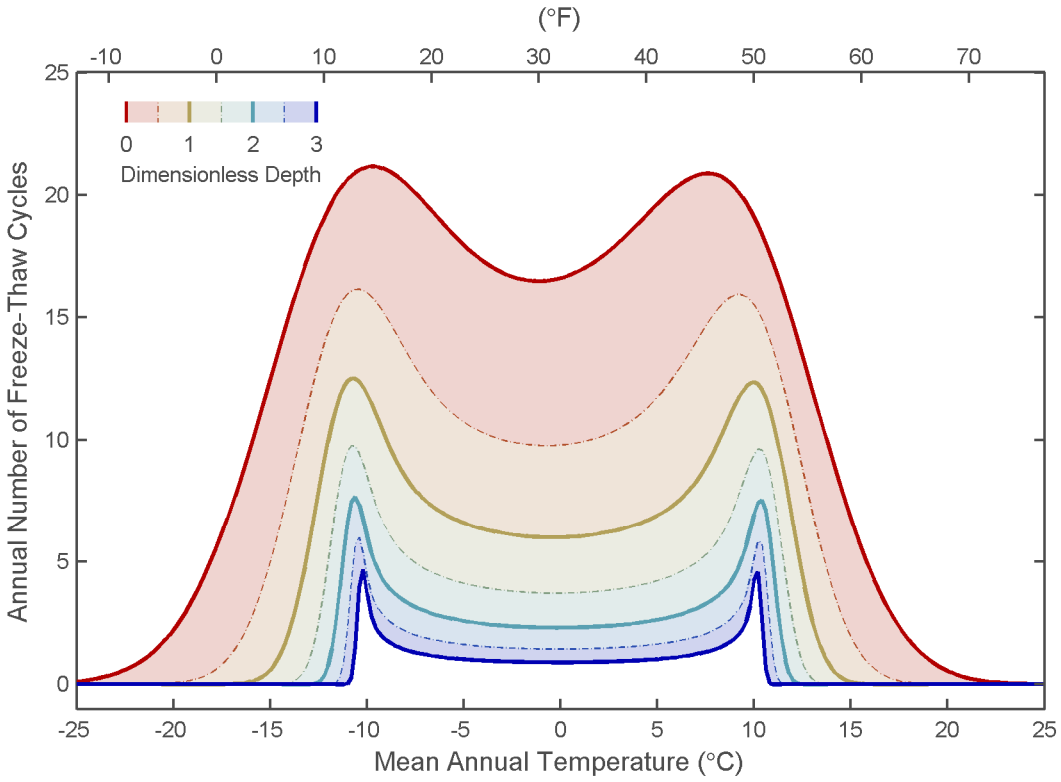

Figure 7-2. Expected Number of Freeze–Thaw Cycles As a Function of Mean Annual Temperature and Dimensionless Depth Below Ground Surface

toward 0 °C [32 °F]. Freeze-thaw cycles are infrequent and penetrate less than 10 cm [4 in] with MAT between 15 and 18 °C [59 and 64 °F], typical of present-day MAT across Yucca Mountain (see Section 5.2). If soil temperatures were 5.6 to 7 °C [10 to 13 °F] cooler, as Stothoff and Walter (2007) estimated for the last glacial maximum, diurnal cycling would be near the theoretical peak. Under this scenario, there might be an annual average of 15 to 20 freeze-thaw cycles at the ground surface and several cycles even 50 cm [20 in] deep within the soil profile. Freeze-thaw weathering would presumably be relatively efficient at Yucca Mountain under such conditions.

Soil temperatures tend to be higher than air temperatures at Yucca Mountain, based on approximately 162 days of observations from 2 pairs of sensors on opposing north-facing/south-facing slopes (both with slope angles of approximately 25°) in Split Wash.[6] North-facing slopes are a few degrees warmer than air temperatures, and south-facing slopes are at least four degrees warmer still. Even under glacial conditions it may be that south-facing Yucca Mountain slopes see minimal freeze–thaw activity. Under current conditions, higher elevations would be expected to exhibit significant freeze–thaw. Rainier Mesa, for example, reaches an elevation of roughly 2,200 m [7,200 ft], which is sufficiently cool that freeze–thaw weathering may be particularly active.

[6]The temperature data was made available by DOE. The data tracking number is GS970908312242.003.

7.1.5 Chemical Weathering

Chemical weathering occurs when rocks and minerals are not in equilibrium with the near-surface water. Reactions occur to yield products that are more stable in near-surface environments. In some cases, minerals go into solution without precipitation of other substances. Otherwise, some or all of the ions released by weathering precipitate to form new compounds (e.g., clay compounds), which can cause volume changes that stress the rock and promote mechanical weathering (Birkeland, 1999). Under present-day arid conditions and in relatively coarse soils, chemical weathering is not a significant factor; thus it is not considered in the computational model. Chemical weathering may be a more significant factor during wetter portions of the glacial cycle.

7.1.6 Bedrock Entrainment

Rock fragments form a significant fraction of the soil column in some locations of Yucca Mountain hillslopes, ranging in size from gravel to tens of centimeters across. Bedrock fracture patterns are a primary determinant of the initial size of rock fragments. Weathering processes active on soil particles are also active in the near-surface environment. The equilibrium model considers bedrock entrainment to provide a relatively small volume source to the soil column relative to dust deposition. The model characterizes bedrock entrainment as exponentially decreasing with soil thickness above the bedrock surface, because the frequency of wetting pulses reaching the bedrock and the magnitude of temperature oscillations both decrease exponentially with soil thickness.

7.2 Computational Soil-Balance Model

The soil-balance model takes into account erosion and sediment transport due to water movement, as well as soil creep and passive degradation. The model only accounts for one generic particle size, given the uniformity of the eolian sands, and does not consider a distribution of particle sizes.

The model does not directly calculate erosion due to rain splash or long-range transport due to gravity (i.e., boulders rolling downhill). In the current implementation, spatial variability of soil thickness arises solely from the variability in surface elevation; all erosion-balance parameters are assumed constant in space.

The current soil distribution on the ridges and hillslopes is considered relatively modern, with much of the Pleistocene soils stripped after the start of the current interglacial period. An important assumption in the modeling is that a quasi-equilibrium condition has been reached, at least for the ridges and hillslopes, and there is little remnant soil. A quasi-equilibrium condition also may have been reached in the wash bottoms, at least in the top of the soil column; however, alluvial fill and terraces represent a sequence of depositional events that cannot be considered with equilibrium modeling.

The classical approach to modeling colluvial redistribution, as exemplified in a DEM-based model presented by Dietrich, et al. (1995), steps through time using a colluvium-diffusion equation. The approach used here, on the other hand, assumes steady-state equilibrium and considers overland sediment flow as well as creep. The soil-balance mathematical model generally follows the approach presented by Beaumont, et al. (1992), with the overland flow and erosion models based upon work presented by Woolhiser, et al. (1990).

Three equilibrium balance equations are solved to calculate the equilibrium thickness of soil over the Yucca Mountain region: (i) overall soil mass balance, (ii) sediment mass balance [Eq. (7-1)], and (iii) hydraulic mass balance for overland flow [Eq. (7-8)]. The overall soil mass balance equation is

$$\nabla \cdot q_{\text{soil}} - Q_{\text{src}} - \overline{Q}_{\text{str}} = 0 \tag{7-17}$$

where

q_{soil} — volumetric soil flux vector [L^3/L^2T]
Q_{src} — soil source from bedrock and dust [L^3/L^3T]
$\overline{Q}_{\text{str}}$ — time-averaged soil source from overland flow [L^3/L^3T]

The erosion-balance model assumes that all processes are at equilibrium. Thus, the streamflow model assumes that a representative spatially uniform rainfall rate is applied over the entire mountain, and the resulting equilibrium hydraulic flux distribution is used to calculate equilibrium sediment transport. Because streamflow is actually highly episodic at Yucca Mountain, the equilibrium sediment-transport velocities and erosion/deposition rates are adjusted to account for time without streamflow. Time-averaged stream-induced flux is approximated here by

$$\overline{Q}_{\text{str}} \approx F_{\text{str}} Q_{\text{str}} \tag{7-18}$$

where F_{str} is the fraction of time streamflow occurs. The soil thickness model uses a characteristic value for F_{str} that balances the different characteristic durations for overland-flow areas, headwater areas, and downstream areas.

Flux of soil, other than through sediment transport, is assumed to occur through viscous creep and is gravity-driven

$$q_{\text{soil}} = -Kb^3 \nabla z = -\frac{\rho g b^3}{3\mu} \nabla z \tag{7-19}$$

where

K — effective conductivity coefficient [1/T]
b — soil thickness [L]
z — ground surface elevation [L]
μ — effective time-averaged viscosity (assumed spatially constant) [M/LT]

The soil-flux term is similar to the short-range transport model used by Beaumont, et al. (1992), except that here b is the variable to be determined and z is constant, while in the Beaumont, et al. (1992) application, z is the variable to be determined and all other variables are assumed constant and lumped into one term. The soil-flux term also differs from the Beaumont, et al. (1992) application by using b^3 (in accordance with film-flow theory) rather than b. Trial tests (not shown) suggested that simulations using b tend to produce estimates of soil thickness increasing downslope more rapidly with distance from the ridgeline than trench observations would support.

The creep conductance depends on several factors. Creep is enhanced by moist conditions, particularly when enough dust is present to lubricate flow of larger particles. As root-length densities increase, however, creep is reduced. Viscosity may vary by orders of magnitude; a time-averaged viscosity is used. In calculating a time-averaged set of properties, it is important to time-average the reciprocal of viscosity. If the reciprocal of viscosity is time-averaged, infrequent low-viscosity and consequently fast events such as slumping contribute to creep transport; otherwise, such events are completely neglected.

A simple source term representing weathering is used here. It is assumed that soil protects the bedrock from physical weathering, and weathering decreases exponentially with soil thickness

$$Q_{\text{wea}} = Q_0 \exp\left(-b / b_0\right) \tag{7-20}$$

where Q_0 is the source strength and b_0 represents a weathering-protection soil thickness. The two fitting parameters, Q_0 and b_0, can be used to match observed soil thicknesses. Note that the number of freeze–thaw cycles in a year decays exponentially with depth below ground surface, consistent with the weathering source term. Particles generated from the bedrock are actually chunks of bedrock rather than grains typical of the fine portion of the soil; consideration of particle size distributions is beyond the scope of the work presented here.

Each of the three balance equations is solved using the same general finite-volume flow-routing approach. The DEM grid is discretized into square cells, with one-dimensional connections to the nearest eight cells (including diagonals). Taking advantage of the hyperbolic nature of the equations by assuming that upstream variables uniquely determine fluxes to downstream cells, the cells in the grid are processed in order of highest to lowest elevation in one pass.

The water-balance equation is solved independently of the sediment- and soil-balance equations. In the water-balance equation, each cell is processed using the algebraic equation

$$A_i q_{\text{rain}} + \sum_{j=\text{up}} \frac{w_{ij} h_j^{5/3}}{n} \left(\frac{z_j - z_i}{\Delta_{ij}} \right)^{1/2} - \sum_{j=\text{down}} \frac{w_{ij} h_i^{5/3}}{n} \left(\frac{z_i - z_j}{\Delta_{ij}} \right)^{1/2} = 0 \tag{7-21}$$

where

i	—	cell being processed
j	—	cell adjacent to cell i
q_{rain}	—	rainfall rate minus infiltration rate [L^3/L^2T]
A	—	grid cell area [L^2]
w_{ij}	—	width of connection between cells I and j [L^2]
Δ_{ij}	—	length of connection between cells i and j [L]

Sums over upstream and downstream cells are denoted by j = *up* and j = *down*, respectively. On a square grid with constant cell spacing Δ, w_{ij} is $\Delta/2$ for nearest-neighbor connections and $\sqrt{2}\Delta/3$ for diagonal connections.